Development/Plasticity/Repair

The Differentiation Status of Hair Cells That Regenerate Naturally in the Vestibular Inner Ear of the Adult Mouse

Antonia González-Garrido,[1] Rémy Pujol,[2,3] Omar López-Ramírez,[1] Connor Finkbeiner,[2] ⬤Ruth Anne Eatock,[1] and Jennifer S. Stone[2]

[1]Department of Neurobiology, University of Chicago, Chicago, Illinois 60637, [2]The Virginia Merrill Bloedel Hearing Research Center and the Department of Otolaryngology Head and Neck Surgery, University of Washington, Seattle, Washington 98195, and [3]Institute for Neurosciences of Montpellier-Institut National de la Santé et de la Recherche Médicale Unit 1052, University of Montpellier, 34091 Montpellier, France

Aging, disease, and trauma can lead to loss of vestibular hair cells and permanent vestibular dysfunction. Previous work showed that, following acute destruction of ~95% of vestibular hair cells in adult mice, ~20% regenerate naturally (without exogenous factors) through supporting cell transdifferentiation. There is, however, no evidence for the recovery of vestibular function. To gain insight into the lack of functional recovery, we assessed functional differentiation in regenerated hair cells for up to 15 months, focusing on key stages in stimulus transduction and transmission: hair bundles, voltage-gated conductances, and synaptic contacts. Regenerated hair cells had many features of mature type II vestibular hair cells, including polarized mechanosensitive hair bundles with zone-appropriate stereocilia heights, large voltage-gated potassium currents, basolateral processes, and afferent and efferent synapses. Regeneration failed, however, to recapture the full range of properties of normal populations, and many regenerated hair cells had some properties of immature hair cells, including small transduction currents, voltage-gated sodium currents, and small or absent HCN (hyperpolarization-activated cyclic nucleotide-gated) currents. Furthermore, although mouse vestibular epithelia normally have slightly more type I hair cells than type II hair cells, regenerated hair cells acquired neither the low-voltage-activated potassium channels nor the afferent synaptic calyces that distinguish mature type I hair cells from type II hair cells and confer distinctive physiology. Thus, natural regeneration of vestibular hair cells in adult mice is limited in total cell number, cell type diversity, and extent of cellular differentiation, suggesting that manipulations are needed to promote full regeneration with the potential for recovery of vestibular function.

Key words: hair cell voltage-gated channels; ribbon synapse; stereocilia; type I hair cell; type II hair cell; utricle

---

Significance Statement

Death of inner ear hair cells in adult mammals causes permanent loss of hearing and balance. In adult mice, the sudden death of most vestibular hair cells stimulates the production of new hair cells but does not restore balance. We investigated whether the lack of systems-level function reflects functional deficiencies in the regenerated hair cells. The regenerated population acquired mechanosensitivity, voltage-gated channels, and afferent synapses, but did not reproduce the full range of hair cell types. Notably, no regenerated cells acquired the distinctive properties of type I hair cells, a major functional class in amniote vestibular organs. To recover vestibular system function in adults, we may need to solve how to regenerate the normal variety of mature hair cells.

Introduction

In most adult nonmammalian vertebrates, the death of inner ear hair cells triggers their regeneration and integration into the sensory system, restoring sensory function. In adult mammals, auditory hair cells are not replaced following damage, for reasons that remain unclear (for review, see Groves, 2010). Vestibular organs in adult rodents and humans do regenerate some hair cells naturally through transdifferentiation of supporting cells (Warchol et al., 1993; Forge et al., 1993, 1998; Kawamoto et al., 2009; Lin et al., 2011; Golub et al., 2012; Slowik and Bermingham-McDonogh, 2013; Taylor et al., 2015; Wang et al., 2015; Bucks et al., 2017; Taylor et al., 2018; Hicks et al., 2020). Nevertheless, extensive bilateral loss of vestibular hair cells in adult humans produces permanent dysfunction, including vertigo, imbalance, and unstable vision (Tsuji et al., 2000; Rauch et al., 2001; Hirvonen et al., 2007; Agrawal et al., 2009; Van Hecke

et al., 2017). In adult rodents with bilateral loss of vestibular hair cells, even with significant regeneration there is little recovery of function, as shown by swim tests (Staecker et al., 2007), vestibulo-ocular reflex (VOR) performance (J. Stone and J. Phillips, unpublished observations), stimulus-evoked vestibular potentials (Sayyid et al., 2019), and vestibular signs such as head bobbing and body circling (Golub et al., 2012).

Why is there no recovery of vestibular function despite the replacement of hair cells? This might reflect insufficient numbers of new hair cells, deficiencies in such basic functions as mechanosensitivity or synaptic transmission, or loss of specific types of hair cells. There is some evidence for the latter. Mammalian vestibular epithelia have two classes of hair cell, type I and type II, which differ strikingly in morphology, molecular markers, ion channel complements, and afferent and efferent synaptic mechanisms (for review, see Eatock and Songer, 2011; Meredith and Rennie, 2016; Burns and Stone, 2017). The hair cells that regenerate in adult rodents are type II like in gross morphology, lacking the distinctive calyceal afferent synapses of type I cells (Forge et al., 1993; Kawamoto et al., 2009; Golub et al., 2012; Sayyid et al., 2019), and, like normal type II but not type I cells, express Sox2 and calretinin (Hicks et al., 2020).

We have been investigating the potential for adult vestibular hair cell regeneration in mice expressing the human diphtheria toxin receptor (DTR) gene in hair cells (Erkman et al., 1996; Xiang et al., 1997). We showed previously that diphtheria toxin (DT) injections in adult DTR mice killed vestibular hair cells rapidly and in large numbers (Golub et al., 2012), inducing head bobbing and circling. Within 60 d, hair cell numbers increased significantly, but there was no evidence for the regeneration of type I cells and no reversal of the vestibular signs. Hair cells that regenerate naturally in damaged cristae and saccules of adult mice also appear to be type II (Hicks et al., 2020). In contrast, DT treatment in neonatal DTR mice (Wang et al., 2019) produced regeneration of both type I and type II hair cells and significant functional recovery as assessed by vestibular evoked potentials (VsEPs). The neonatal mouse inner ear corresponds developmentally to second-trimester human embryos (Pujol et al., 1997). Understanding the nature of the loss of regenerative capacity in adults is critical for restoring function to mature human vestibular inner ears.

Here we look more closely at hair cells that regenerate in adult DTR mice following DT treatment, extending the time for regeneration to >1 year. We ask whether individual regenerated hair cells have basic functionality (mechanosensitivity, voltage-gated currents, and synapses) and whether signs of differentiation into hair cell types have been missed. We focus on the utricle, which detects linear acceleration and head tilt, and is a model for genetic, molecular, and electrophysiological studies. Control and regenerated hair cells are compared for molecular markers, ultrastructural features of hair bundles and synapses, and electrophysiological properties. We report that the regenerated hair cells acquired key similarities to normal adult hair cells but also differed in ways that may contribute to the persistence of systems-level dysfunction.

Materials and Methods

Animals
For most experiments, mice were $Pou4f3^{DTR+/-}$ (DTR) or $Pou4f3^{DTR+/+}$ [wild type (WT)]. Mice were housed at the University of Washington and the University of Chicago. In experiments on mechanotransduction currents, the experimental mice were DTR mice, and the control mice were WT C57BL/6J, the background strain of the DTR mice. All

procedures were conducted in accordance with approved animal protocols from the Institutional Animal Care and Use Committees from the respective university.

In the study by Golub et al. (2012), we assessed hair cell regeneration in utricles of adult DTR mice on either C57BL/6J or mixed (C57BL/6J plus 129SV) genetic background. For the current study, we used DTR mice on a C57BL/6J background or a different mixed genetic background (C57BL/6J plus CBA/CaJ). We confirmed that the mice we used here share the key results reported by Golub et al. (2012): in adult mouse utricles, only ~5% of the total hair cell population survives DT, the regenerated hair cells are type II like in their gross morphology and lack of calyceal contacts, and the number of regenerated hair cells reaches a maximum by ~70 d post-DT treatment.

We also looked into using DTR mice on a CBA/CaJ background but found that the same dose of DT caused a much smaller lesion, with higher numbers of surviving hair cells. One round of backcrossing the CBA/CaJ mice to C57BL/6J mice restored the original sensitivity to DT and full-sized lesions. Therefore, CBA/CaJ mice were not used in this study.

Diphtheria toxin administration
Experimental mice (DTR mice; age, 6–9 weeks) received two intramuscular injections of DT from Sigma-Aldrich or List Biological Laboratories at 25 ng/g, spaced 2 d apart. Control animals were as follows: (1) mice with no DTR allele that received DT injections (called WT); and (2) mice with no DTR allele that received no DT injection (called WT-no DT). Time after DT injection is specified as "days post-DT."

DT potency varied across batches and with time stored at –20°C. At the time of delivery of each new shipment of DT and every 4–6 months thereafter, we verified DT potency relative to published effects of DT on adult DTR mice (Golub et al., 2012) by comparing, in one to two DTR mice from a given cohort at 14 d post-DT, the following: (1) hair cell destruction; and (2) behavioral changes indicating vestibular dysfunction (i.e., postural defects, head bobbing, and circling).

Morphologic studies
WT and DTR mice were killed by CO_2 gas overdose at 14, 28, 42, 70, 100, 140, or 170 d post-DT. Some were WT-no DT mice and had similar ages to mice in the other two groups. Utricles were prepared for immunolabeling and confocal microscopy, or for transmission electron microscopy (TEM).

Tissue labeling for confocal microscopy. Each temporal bone was isolated, and utricles were fixed by creating a small hole in the otic capsules over the utricles and infusing 4% buffered paraformaldehyde (PFA) through the hole into the perilymphatic space for 1 min. The temporal bone was then immersed in PFA for 2 h at room temperature, then rinsed in PBS. Utricles were then dissected out and otoconia were removed. Whole utricles were immunolabeled free floating using standard techniques (for details, see Bucks et al., 2017) with the following primary antibodies: rabbit anti-myosin VIIa (1:100; catalog #25–6790, Proteus Biosciences; RRID:AB_10015251); mouse anti-Ctbp2 IgG1 (1:500; catalog #612044, BD Biosciences; RRID:AB_399431); and mouse anti-GluA2 (GluR2) IgG2a (1:500; catalog #MAB397, Millipore; RRID: AB_2113875). Some utricles were also labeled for filamentous actin with 10 μg/ml phalloidin (Alexa Fluor 594, Thermo Fisher Scientific) dissolved in PBS plus 0.5% Triton X-100 (catalog #9002–93-1, Sigma-Aldrich). All utricles were counterlabeled with the nuclear stain 4′,6′-diamidino-2-phenylindole dihydrochloride (DAPI). Finally, tissue was mounted onto glass slides using FluoroMount-G mounting media (catalog #F4680, Sigma-Aldrich) and coverslipped. Slides were stored at 4°C.

Confocal microscopy. Immunolabeled utricles were examined with a confocal laser scanning microscope (model FV1000, Olympus) at 60× or 100× (under oil) at 1–3× zoom. Images were captured as z-stacks with 0.5 or 1 μm steps, starting apically at the stereocilia and extending basally through the basal lamina of the sensory epithelium. Images were processed with Fiji software (https://imagej.net/software/fiji/).

Transmission electron microscopy. We rapidly exposed the temporal bone and introduced fixative (2.5% glutaraldehyde/0.2 M cacodylate

buffer) through a small hole above the utricle. The temporal bone was then removed and placed in fixative for further dissection. Isolated utricles were immersed in fresh fixative (2 h to overnight) at 4°C, post-fixed with 2% osmium tetroxide in cacodylate buffer for 1 h, rinsed in the same buffer, and stored at 4°C until embedding. Utricles were then dehydrated and embedded in plastic (Eponate; catalog #18010, Ted Pella). Blocks were trimmed and oriented to give semi-thin (2 µm) transverse sections. Sections were labeled with toluidine blue (catalog #T3260, Sigma-Aldrich), dried, and coverslipped in DPX Mounting Medium (catalog #13412, Electron Microscopy Sciences). Ultrathin (80–90 nm) sections were collected on mesh or Formvar-coated grids. Several series of thin sections, separated by 10–15 µm, were taken throughout each utricular sensory epithelium (macula) to allow visualization of zones: the central strip, called the striola, and the surrounding zone, called the extrastriola, which has a lateral subzone [lateral extrastriola (LES)] and a medial subzone [medial extrastriola (MES)]. Cytoarchitectural differences between the striola and extrastriola correlate with differences in afferent physiology (for review, see Goldberg, 2000; Eatock and Songer, 2011). Most of our TEM measurements were taken from the LES, where the density of regenerated hair cells is highest (Golub et al., 2012). Sections were imaged with a transmission electron microscope (model 1230, JEOL) equipped with a digital camera (model XR80, AMT).

Quantitative morphologic analyses
We performed morphologic analyses on utricles from WT and *DTR* mouse groups using confocal microscopy or TEM. We noted no differences between WT mice that were injected with DT and WT-no DT mice. Therefore, we included both kinds of WT controls and identified which kind was used for each analysis. For qualitative analyses of hair cells and afferent neural elements in the sensory epithelium, we examined two to four mice per group and per time point. Quantitative analyses were performed as follows.

Stereocilium diameter. From high-magnification transmission electron micrographs, we measured the diameter of two to three stereocilia per hair cell at 1–2 µm from their insertion point in the cuticular plate and computed the average diameter for the three stereocilia (see Fig. 4). For each time point, we measured the stereocilium diameter of type II hair cells from WT-no DT mice and *DTR* mice at 28, 42, 70, and 140 d post-DT. For comparison, we also measured the diameter of type I hair cell stereocilia and supporting cell microvilli from WT-no DT mice.

Tallest stereocilium height. We measured the height of the tallest stereocilia in each hair bundle from both confocal and transmission electron micrographs (see Fig. 4). We took confocal images (60× oil immersion, 2–3× zoom) from the LES of utricles for which stereocilia were labeled with the F-actin label, phalloidin, and hair cells were labeled with myosin VIIa antibody. We used Fiji or Photoshop (Adobe Systems) to measure the distance from the cuticular plate (into which stereocilia are inserted) to the tip of the tallest stereocilia on regenerated type II hair cells and on surviving type I hair cells. Because stereocilia were bent at different angles in our samples, our measurements may underrepresent stereocilia height by varying amounts. In *DTR* mice, we used confocal microscopy to measure the tallest stereocilia of regenerated hair cells and of surviving (not regenerated) type I hair cells at 70 and 170 d post-DT. Using TEM, we measured the tallest stereocilia of normal type I and II hair cells in WT-no DT mice and of regenerated hair cells in *DTR* mice at 70 and 170 d post-DT.

Hair bundle orientations. Montages of entire utricular epithelia were made for two *DTR* mice at 170 d post-DT. Confocal images were taken at 60× and the montages were constructed in Photoshop. Hair cell cuticular plates and stereocilia were labeled with phalloidin, leaving an unstained circle (hole) corresponding to the kinocilium (a true cilium with microtubules rather than F-actin). For each hair cell, we estimated hair bundle orientation as the vector bisecting the hair bundle and running from its shortest row of stereocilia toward the tallest stereocilia and the kinocilium. Findings were similar for the two montages; the map of bundle orientations for one montage is shown in Figure 3B.

Colocalization of presynaptic and postsynaptic elements of ribbon synapses. We localized hair cell-afferent synapses by colabeling utricles with antibody against Ctbp2, a protein in presynaptic ribbons in hair cells, and antibody against postsynaptic glutamate (GluA2) receptors in the afferent terminals. Close apposition of the two labels was taken to indicate the presence of a functional synapse, and we compared the percentage of such functional synaptic contacts for WT type II and *DTR* regenerated hair cells (see Fig. 8). Confocal images (100× oil immersion, 4× zoom) were taken from the LES region of utricles immunolabeled for myosin VIIa, Ctbp2, and GluA2. With Huygens Professional software (version 15.5; Scientific Volume Imaging), we segmented the basolateral processes of hair cells, where most synapses are found (Pujol et al., 2014), and identified sites of closely apposed Ctbp2 and GluA2 labels with the colocalization function. Standardized thresholding and watershedding were used to define Ctbp2-labeled ribbons and GluA2-labeled plaques. We analyzed the following groups: WT-no DT mice, WT mice at 170 d post-DT, and *DTR* mice at 170 d post-DT.

Ribbon synapse density. At two different times post-DT, in both WT and *DTR* utricles, we measured the volume occupied by the myosin VIIa$^+$ basolateral processes of type II hair cells in a confocal *z*-series image (see Fig. 8). Density was calculated by dividing the number of Ctbp2-labeled ribbons by the basolateral process volume. We analyzed WT and *DTR* mice, both at 42 and 170 d post-DT.

Ribbon synapse maturity. Using high-magnification transmission electron micrographs, we assessed the relative number of ribbons at synapses versus ribbon precursors. Ribbons at synapses were defined as follows: surrounded by synaptic vesicles, located adjacent to the plasma membrane, and apposed to a postsynaptic density on an afferent bouton. Ribbon precursors were defined as follows: located within the cytoplasm, not adjacent to the plasma membrane, and lacking synaptic vesicles. For this analysis, we assessed WT-no DT mice, *DTR* mice at 28–42 d post-DT, and *DTR* mice at 140–170 d post-DT (see Fig. 9).

Electrophysiology
Preparation. The *Pou4f3$^{DTR+/-}$* (*DTR*) and *Pou4f3$^{DTR+/+}$* (WT) mice were obtained from the University of Washington and bred at the University of Chicago. The data on voltage-gated currents (see Figs. 6, 7, 11) are from WT ($n = 6$ mice) and *DTR* ($n = 22$ mice) littermates that were injected with DT at 6–9 weeks of age, as described above, and maintained postinjection (post-DT) for times ranging from 14 to 451 d. For the data on mechanoelectrical transduction (see Fig. 5), the experimental mice were 8 of the 22 *DTR* mice, and the control animals were 4 mice of the background strain (C57BL/6J) with no DT treatment.

On the day of recording, utricles were excised and prepared for whole-cell patch recordings as described previously (Rüsch and Eatock, 1996; Vollrath and Eatock, 2003). Briefly, animals were deeply anesthetized and decapitated, and the utricles were rapidly excised into Leibovitz-15 (L15) medium modified by adding 10 mm HEPES (~315 mmol/kg, pH 7.4). Chemicals were obtained from Sigma-Aldrich, unless otherwise specified. The utricular sensory epithelium (macula) was trimmed and briefly exposed to protease XXIV [100 mg/ml at room temperature (24–27°C)] to facilitate gentle removal of the otolithic membrane covering the hair bundles. The epithelium was mounted apical surface up in a recording chamber on a microscope (model Axioskop FS, Zeiss) with differential interference contrast and fluorescence optics. In some experiments, the superior division of the vestibular ganglion and distal part of the vestibular nerve were included in the preparation, preserving afferent terminals (Songer and Eatock, 2013).

Recordings. Whole-cell GΩ-seal recordings were made at room temperature with pipettes of 3–5 MΩ resistance in standard solutions. In most experiments, the bath (external) solution was the supplemented L15 medium described above. The pipette (internal) solution was a conventional KCl solution, as follows (in mm): 135 KCl, 0.1 CaCl$_2$, 3.5 MgCl$_2$, 3 Na$_2$ATP, 5 creatine phosphate (Na salt), 0.1 NacAMP, 0.1 Li-GTP, 5 EGTA, and 10 HEPES, plus ~28 mm KOH to bring pH to 7.3 and osmolality to ~300 mmol/kg. Sulforhodamine 101 (1 mg/100 ml; Thermo Fisher Scientific) added to the standard internal solution filled each recorded cell with fluorescent label for visualization. The patch-clamp amplifier with integrated digital (D)-to-analog (A) and A/D converter (model EPC-10, HEKA Elektronik) was controlled by Patchmaster software (https://heka.com/). Whole-cell currents evoked by voltage steps were recorded with the amplifier low-pass corner
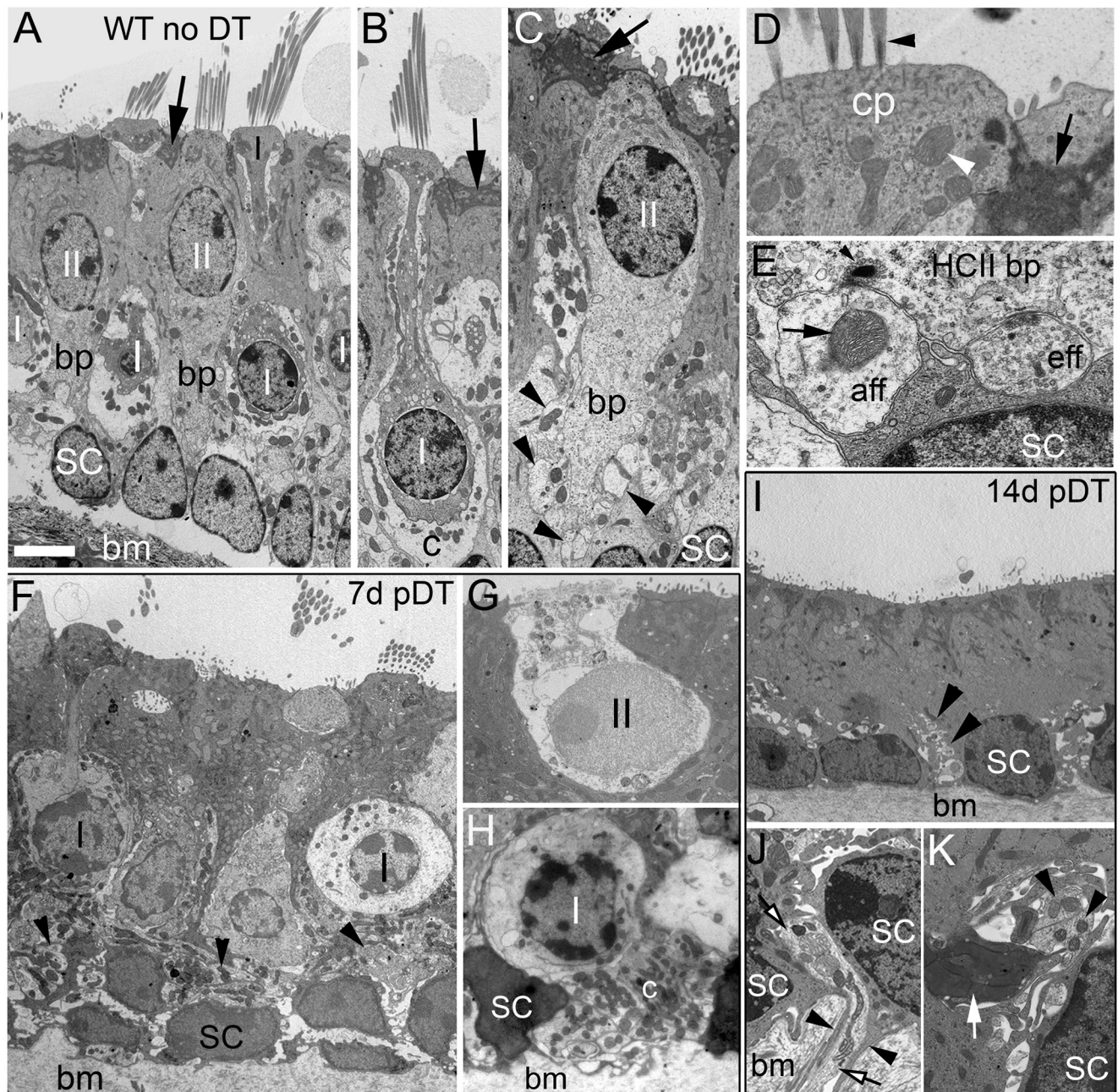
Figure 1. DT induces destruction of type I and II hair cells and degeneration of calyx afferent terminals. *A–K*, Transverse TEM sections from WT utricular maculae (*A–E*) and *DTR* maculae (*F–K*) at early stages post-DT treatment. The apical (lumenal) surface of the epithelium is toward the top. Overlying otolithic accessory structures have been dissected away. *A–E*, Adult WT-no DT utricular maculae, showing type I (I) and type II (II), hair cells, supporting cells (SC), region of basement membrane (bm), and neural elements, including afferent calyces (c). In *A–D*, black arrows point to apices of supporting cells, which separate the hair cells. *A*, Type II hair cells have basolateral processes (bp) that extend from below the layer of type II nuclei toward the more basal layers of type I and SC nuclei. *B*, Type I hair cell surrounded by an afferent calyx. *C*, Type II hair cell with large basolateral process contacted by multiple afferent boutons (arrowheads). *D*, High-magnification image of the top of a type II hair cell showing insertion of stereocilia (black arrowhead) into the apical cuticular plate (cp). White arrowhead, Mitochondrion; black arrow, electron-dense material near apex of supporting cell. *E*, An afferent bouton (aff) and an efferent varicosity (eff) apposed to basolateral process of a type II hair cell. Arrow, Mitochondrion in afferent bouton; arrowhead, electron-dense synaptic ribbon and associated synaptic vesicles, in the hair cell. *F–K*, Adult *DTR* utricular maculae at early times post-DT. *F–H*, Degenerating hair cells at 7 d post-DT, with misshapen cell bodies and nuclei. *F*, Arrowheads point to neurites. *G*, Type II hair cell undergoing cytolysis, with considerable loss of organelles and nuclear chromatin. *H*, Type I hair cell with its nucleus displaced more basally than normal—see basement membrane and supporting cell nuclei. Note pyknotic nucleus, cytoplasmic vacuoles, and remnants of the retracted calyx (c) filled with mitochondria. *I–K*, DTR epithelia at 14 d post-DT. *I*, At 14 d post-DT, the macula is very thin and devoid of hair cells (note complete absence of stereocilia). Small neurites are surrounded by supporting cells or interstitial fluid (arrowheads). *J*, Basal end of the epithelium at high magnification. A neurite (white arrows with black outline) passes through the bm and into the sensory epithelium, passing two SC nuclei. Thin cytoplasmic extensions from each supporting cell (black arrowheads) descend into the basement membrane, enwrapping the neurite. *K*, High-magnification view of neurites near a SC nucleus. Black arrowheads, Healthy-appearing neurites; white arrow, presumed degenerating calyx, filled with dark, swollen mitochondria. Scale bars: *A* (for *A, B, F, I*), 6 µm; *C*, 4 µm; *D*, 1 µm; *E*, 500 nm; *G, H*, 2.6 µm; *J, K*, 1.3 µm.

frequency set at 6 kHz and a sampling interval of 5–20 µs. Capacitive currents were nulled electronically. Series resistances ranged from 4 to 21 MΩ (mean, 9.7 ± 0.4 MΩ; *n* = 57) and were compensated 80.1 ± 0.2% for a mean residual value of ∼2 MΩ. Voltage responses

to iterated current steps were recorded in current-clamp mode. Potentials are corrected for a liquid junction potential of 4 mV, calculated with JPCalc software (Barry, 1994) as implemented by Clampex 10 (Molecular Devices). Cells were held at −64 mV (voltage

clamp) and zero-current potential (current clamp) unless otherwise noted.

Mechanical stimulation. Hair bundles were deflected with a rigid glass probe coupled to a piezoelectric bimorph element driven by voltage (Corey and Hudspeth, 1980) as described in the study by Vollrath and Eatock (2003). Displacement of the probe (in micrometers) per volt was calibrated offline. The driving voltage protocol was a series of sinusoidal bursts (five cycles each) of constant amplitude and incremented in frequency from 2–100 Hz (Songer and Eatock, 2013).

Analysis. Voltage dependence of whole-cell currents was quantified by constructing activation (conductance–voltage) curves from data collected during standard voltage protocols that activate the key currents for immature and mature type II hair cells: currents through outwardly rectifying K channels and voltage-gated Na (Na_V) currents, which are activated by depolarization, and hyperpolarization-activated cyclic nucleotide-gated (HCN) currents, which are activated by hyperpolarization. From a holding potential of -64 mV, the protocol comprised (1) a 50 ms prepulse to -124 mV, to activate HCN current and both deactivate and deinactivate K^+ and Na_V currents; (2) an iterated series of 200 ms test steps; and (3) a 50 ms step to return to holding potential.

For the large outwardly rectifying K^+ currents (I_K), steady-state conductance values were calculated from tail currents at 200 ms when voltage was stepped to -39 mV, divided by driving force (the difference between voltage (V) and the current reversal potential), averaged across all cells, plotted against the test step voltage, and fitted with a Boltzmann function (Eq. 1), as follows:

$$G(V) = \frac{G_{min} - G_{max}}{1 + e^{(V - V_{1/2})/S}} + G_{max} \qquad (1)$$

where $G(V)$ is conductance (G) at V, G_{min} and G_{max} are minimum and maximum currrents, $V_{1/2}$ is voltage corresponding to half-maximal activation, and S is the voltage range corresponding to an e-fold increase in $G(V)$.

For Na_V currents (I_{Na}), we generated activation curves by measuring peak inward current at the onset of iterated voltage steps, dividing by the driving force at each voltage ($V - E_{Na}$, with $E_{Na} = +50$ mV), which were well isolated in time from the slower I_K. We also generated inactivation curves from the fast inward current at the onset of tail current at -39 mV. Here the transient I_{Na} was isolated from I_K by voltage – at those test step voltages that activated I_K, the test step inactivated I_{Na}.

Curve fitting and statistical analyses were performed with OriginPro software (OriginLab). Parameters of curve fits ($V_{1/2}$, G, S) were compared for WT hair cells and *DTR* littermates that underwent identical treatments with DT.

Experimental design and statistical analyses

Data are expressed as the mean $\pm$ SE. The significance of differences between means was assessed by two-sample t tests and ANOVAs followed by *post hoc* Tukey's tests of significance. Distributions were tested for normality and homogeneity of variance. If variance was nonhomogeneous, we applied a Kruskal–Wallis ANOVA followed by Dunn's test of significance. Effect size was estimated with Cohen's d formulation.

Results

We compared ultrastructural and physiological markers of hair cell type in control and regenerated hair cells to determine (1) how well regeneration in adult vestibular epithelia recapitulates the normal differentiation of type II hair cells and their synaptic contacts; and (2) whether, despite the absence of calyces on regenerated hair cells, there are other signs of differentiation into type I cells.

The ultrastructure of regenerated hair cells was type II like

Previous studies have established how to distinguish supporting cells, type I hair cells, and type II hair cells in developing and adult vestibular epithelia of rodents (Nordemar, 1983; Lysakowski and Goldberg, 1997; Forge et al., 1998; Rüsch et al., 1998; Denman-
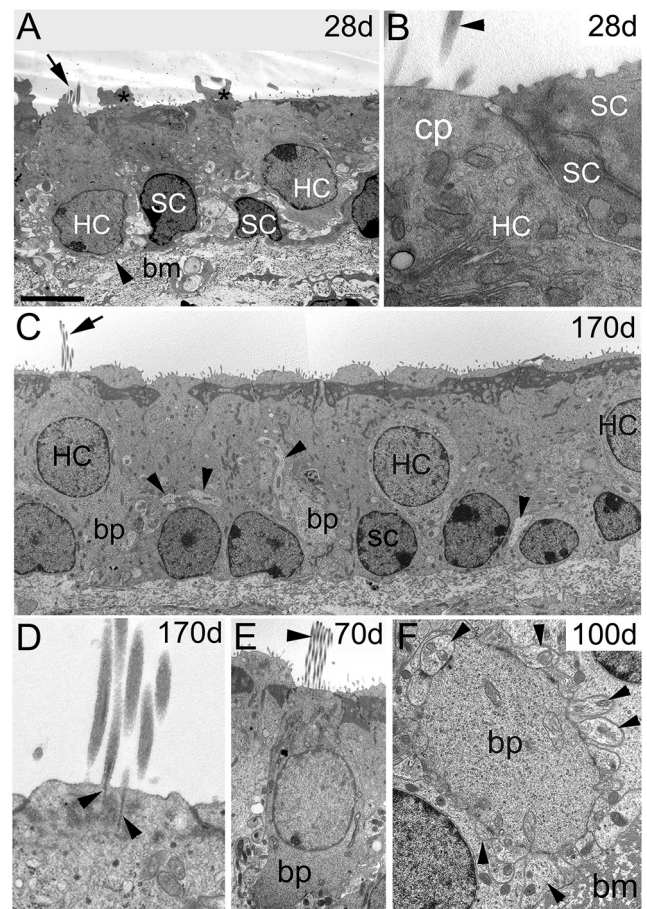

Figure 2. All hair cells regenerated after DT treatment had ultrastructural features of type II hair cells. Transverse sections through utricles from *DTR* mice at different times from 28 to 170 d post-DT. ***A***, At 28 d post-DT, two regenerated hair cells (HC) with basal nuclei, separated by two supporting cells (SC). Arrow, Bundle of short stereocilia; arrowhead, thin strip of supporting cell cytoplasm between the hair cell and the basement membrane (bm); asterisks, cytoplasmic blebs on top of SCs, seen in some specimens. ***B***, High-magnification image of the left HC in ***A*** and two SCs, from a section adjacent to section in ***A***. Stereocilia (arrowhead) emerge from an immature-appearing cuticular plate (cp). ***C***, At 170 d post-DT, regenerated hair cells occupy a distinct layer above the SC nuclei and have multiple mature features. The left hair cell has a fully developed apical pole with a mature-appearing hair bundle (arrow), and a large basolateral process (bp) extending to the basal lamina. Another bp is evident in the center of the panel. Note the numerous healthy neurites (arrowheads). ***D***, Hair bundle of a regenerated hair cell at 170 d post-DT showing well developed stereocilia rootlets (arrowheads) inserted into the cuticular plate. ***E***, Regenerated hair cell at 70 d post-DT with a well formed bundle of stereocilia (arrowhead) and bp. ***F***, The bp of a regenerated type II hair cell at 100 d post-DT located near the bm and surrounded by numerous afferent boutons, some indicated by arrowheads; compare with Figure 1C from an undamaged mouse. Scale bars: ***A***, ***C***, 6 μm; ***B***, ***D***, 1 μm; ***E***, 5 μm; ***F***, 1.5 μm.

Johnson and Forge, 1999; Pujol et al., 2014; Warchol et al., 2019). Our ultrastructural analyses focused on cells in the LES, where the highest density of regenerated hair cells is found after DT-mediated damage (Golub et al., 2012).

In Figures 1 and 2, key features of extrastriolar hair cells, supporting cells, and vestibular nerve endings are illustrated for undamaged (WT-no DT) utricles (Fig. 1A–E) and compared with *DTR* mice at early times post-DT (7–14 d; Fig. 1F–K) and at later times (28–170 d; Fig. 2). In the LES of undamaged mice (Fig. 1A), the sensory epithelium was stratified, with supporting cell nuclei the most basal, type II hair cell nuclei most apical, and type I nuclei in between. Type I and II hair cells bore an apical hair bundle (several linked stereocilia, rooted in the cuticular plate; Fig. 1A,B,D). Type I hair cells had a flask shape, with a

narrow neck connecting the nuclear region to the apical, hair bundle-bearing surface (Fig. 1A,B). Type II hair cells lacked a highly constricted neck and usually had one or more basolateral process (Fig. 1A,C,E). Supporting cells had electron-dense cytoplasm near their apical surfaces (Fig. 1A–D, arrows), their supranuclear cytoplasm was filled with secretory granules (data not shown), and their nuclei were less round than hair cell nuclei and sat more basally in the epithelium (Fig. 1A). Stereocilia varied in dimensions across the epithelium but were shorter and thinner in type II hair cells than in nearby type I hair cells (Fig. 1A). Mitochondria were numerous just below the cuticular plate (Fig. 1D). The cytoplasm of all hair cells had a heavy and even distribution of polyribosomes, making them more electron dense than neural processes, including the calyx (Fig. 1B) and bouton (Fig. 1C,E) contacts that afferents form on type I and type II hair cells, respectively. Figure 1E shows an afferent bouton and an efferent varicosity in contact with a type II hair cell basolateral process. The hair cells had specialized transmitter release sites, called synaptic ribbons, opposite both bouton contacts (Fig. 1E) and calyceal afferent contacts, and efferent nerve endings made synaptic contacts with the basolateral processes of type II hair cells (Fig. 1E) and with afferent terminals, including calyces. We could distinguish afferent boutons from efferent varicosities by the following previously described differences: afferent boutons often had large mitochondria and vesicles that were few and variable in size and density, while efferent varicosities had few mitochondria and numerous vesicles that were consistent with synaptic vesicles given that they had uniform electron density and size, and were clustered opposite a postsynaptic cistern in the hair cell.

For comparison with undamaged utricles, we examined utricles from *DTR* mice between 7 and 170 d post-DT. At 7 d post-DT (Fig. 1F–H), degeneration of both hair cell types was evident, and normal-appearing hair cells were rarely encountered. Hair cells had misshapen nuclei and/or condensed chromatin. The positions of some hair cells were abnormal; for example, a basally displaced cell body of a degenerating type I hair cell is shown in Figure 1H. The shape of hair cells changed as well (Fig. 1, compare *F, A–C*). Hair cell death took both cytolytic (Fig. 1G) and apoptotic (Fig. 1H) forms. For some type I hair cells, the calyx had retracted from the neck and perinuclear area (Fig. 1H). Supporting cells expanded to fill in the spaces where hair cells were lost or shrunken, but they otherwise appeared normal.

At 14 d post-DT, we rarely detected either normal (undamaged control) or degenerating hair cells, and did not see any regenerating hair cells (Fig. 1I), consistent with previous work showing that the number of utricular hair cells decreases by 94% at this time (Golub et al., 2012). The loss of hair cells was accompanied by a dramatic thinning of the epithelium (Fig. 1, compare *I, A*). Neurites in the basal epithelium were enwrapped by supporting cell cytoplasm, even as they penetrated the basement membrane (Fig. 1J, K). Some neurites appeared healthy (Fig. 1K, black arrowheads), while others, full of swollen and dark mitochondria, were likely the remnants of retracted calyces (Fig. 1K, white arrow).

Consistent with previous light microscopic observations on *DTR* utricles (Golub et al., 2012), regenerating hair cells were evident in TEM by 28 d post-DT (Fig. 2A,B). These cells were not likely to be survivors of the DT treatment, which was previously shown to rapidly reduce hair cell numbers by 94% (Golub et al., 2012). They showed no signs of degeneration: their nuclei were spherical or ovoid with a smooth nuclear membrane and normal-appearing chromatin (Fig. 2A). They had such typical hair cell features as abundant polyribosomes, mitochondria below a developing cuticular plate, and stereocilia, and lacked typical supporting cell features such as secretory granules and apical electron-dense material (Fig. 2B). Features signaling that they were immature hair cells included the very basal location of nuclei, almost at the basement membrane (Fig. 2A), and their short stereociliary bundles (Fig. 2A; also see Fig. 4C). With longer time post-DT (70–170 d post-DT; Fig. 2C–F), the new hair cells acquired more mature features, including more apical nuclei and well formed stereocilia and cuticular plates (Fig. 2C–E). They also extended basolateral processes that were contacted all around by afferent bouton terminals (Fig. 2F), as also seen in control mature type II hair cells (Pujol et al., 2014).

In summary, the TEM analysis supports previous studies that concluded that DT treatment rapidly kills virtually all type II hair cells, such that type II-like hair cells seen after 14 d post-DT are newly generated. A small number of type I hair cells did survive DT treatment, as illustrated in later figures (see Figs. 4F, 11).

Regenerated utricles had appropriate hair bundle orientations and overlying accessory structures

A hair cell is excited by deflections of its hair bundle parallel to its orientation axis: a line bisecting the hair bundle and running from the shortest row of stereocilia toward the tallest row. In vestibular hair bundles, a single true cilium, the kinocilium, is linked to the tallest stereocilia and to overlying accessory structures. In otolith organs, the hair bundles reverse orientation at the line of polarity reversal (LPR), which in the mouse utricle runs very near the lateral edge of the striola (Li et al., 2008; Hoffman et al., 2018). In mature utricles, the average orientation of hair bundles is, at any location, toward the LPR; as the LPR curves through the epithelium, the bundles preserve their average orientation relative to the LPR and so gradually change their average absolute orientation. To determine whether the regenerated hair bundles in *DTR* utricles establish the expected mature orientations, we labeled two *DTR* utricles at 170 d post-DT with phalloidin, which stains the filamentous actin of stereocilia and the cuticular plate in which the stereocilia are embedded. The location of the microtubule-based kinocilium, revealed by a hole in the phalloidin stain, provides the orientation of the hair bundle (Fig. 3A). Regenerated hair cells had hair bundles with location-appropriate orientations (Fig. 3B) and average orientation directed toward the LPR, as is normal. The local variability in orientation is not obviously different from that in control adult mice (Li et al., 2008, their Fig. 3).

In otolith organs, hair bundles are surmounted by an "otolithic membrane," a gel layer with embedded crystalline otoconia. During head motions, the relatively dense otoconia lag the motion of the underlying epithelium, displacing the tips of the hair bundles relative to their bases and stimulating transduction by the hair cells. At 170 d post-DT, regenerated utricles had otoconial membranes and otoconia that appeared comparable to those in WT mice (Fig. 3C,D). We do not know whether these structures were retained through the damage or had degenerated and been regenerated. These transverse views also show that the epithelium was much thinner in *DTR* utricles than in WT utricles, as comparison of transmission electron micrographs also showed (compare Figs. 1A, 2C).

Regenerated hair bundles resembled WT type II hair bundles in stereocilia dimensions

Hair bundles house the mechanoelectrical transduction channels and gating springs, and their form varies systematically with developmental stage and hair cell type. During normal
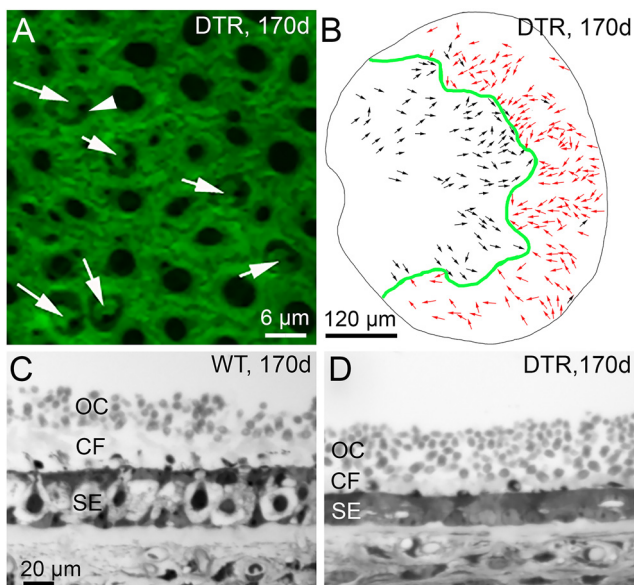
Figure 3. The map of hair bundle orientations and the otoconial layer appeared normal in regenerated DTR utricles. **A**, Hair bundle orientation was visualized by phalloidin labeling of filamentous actin at the apical surface of the utricular macula. A dense network of F-actin in the junctional complexes of supporting cells is punctuated by holes that, in six cases (white arrows), reveal the actin-containing cuticular plates of regenerated hair cells. Arrowhead points to the black hole (lack of stain) at the site of the microtubular kinocilium to one side of a stereociliary bundle. White arrows show the orientations of each hair bundle (see text). **B**, Map of regenerated bundle orientations for one *DTR* utricle: green line, LPR; black arrows, orientations pointing from medial to lateral (left to right); red arrows, orientations pointing lateral to medial. Most orientations were expected for their location relative to the LPR; several black arrows lateral to (right of) the LPR show exceptions. **C**, **D**, Transverse sections through WT (**C**) and DTR (**D**) utricles at 170 d post-dT show otoconia crystals (OCs) and column filament (CF) material above the sensory epithelium (SE). Scale bar: **C** (for **C**, **D**), 20 μm.

development, fine apical microvilli of immature hair cells, similar to microvilli on supporting cells of the sensory epithelium, are gradually replaced by a highly ordered array of rows of taller, thicker, and specialized microvilli, called stereocilia (Denman-Johnson and Forge, 1999; McGrath et al., 2017), which are rich in actin and house the mechanotransduction channels. We used confocal and transmission microscopy to examine whether the regenerated hair cells developed stereocilia with the typical dimensions of mature WT hair bundles, and if so, whether they were type II like or type I like, with taller and thicker dimensions.

Figure 4A shows a mature type II hair bundle from a WT-no DT mouse, viewed from the side in a transverse transmission electron micrograph to reveal multiple stereocilia arranged in a staircase of rows of ascending height. The arrow points to the insertion site of the stereocilia in the cuticular plate. In *DTR* mice at 7 d post-DT, fused stereocilia, a sign of damage, were common (Fig. 4B). On regenerated hair cells at an early stage of regeneration (*DTR* mice at 28 d post-DT), new stereocilia were evident (Fig. 4C). By 70–170 d post-DT in *DTR* mice, stereocilia resembled WT stereocilia in height and diameter (Fig. 4D,E), had acquired a staircase arrangement (Fig. 4E), and had formed a mature-looking cuticular plate (Fig. 4E).

To quantify these observations, we used confocal and transmission microscopy to measure the heights of the tallest stereocilia per bundle in regenerated hair cells of *DTR* mice at 70 and 170 d post-DT, and TEM to measure stereocilia diameter in WT-no DT hair cells and *DTR* hair cells at multiple stages of

regeneration. For confocal measurements of stereocilia height in whole-mounted utricles, we labeled hair cells with antibodies to myosin VIIa, which labels their cytoplasm, and bundles with phalloidin, which stains the filamentous actin that forms the stereociliary cores. Then, we measured the distance from the base of the hair bundle to its apex (Fig. 4F, regenerating bundle). Because the view was somewhat oblique, our measurements tended to underestimate height. In WT preparations, hair bundles were dense and occluded each other, making it difficult to measure bundle heights. Instead, we used transmission electron microscopy to measure, in transverse sections, the height of the tallest stereocilia of WT hair cells. We also measured hair bundle heights from transmission electron micrographs of *DTR* epithelia, for both regenerated hair cells and the rare surviving type I hair cells (Fig. 4F), allowing further comparisons. Height measurements are summarized in Figure 4G.

Measured heights for both WT-no DT type II and regenerated hair bundles fell between 3 and 6 μm. Differences were tested among WT-no DT type II and regenerated bundles at different ages with one-way ANOVA and *post hoc* Tukey's means comparisons. No significant differences were detected between the WT type II samples (mean ± SEM, 4.61 ± 0.27 μm; $n = 8$ bundles) and each of the samples of regenerated bundles (70 and 170 d post-DT, TEM, and confocal; Fig. 4G), or the grand mean for all 67 regenerated bundles [mean ± SEM, 4.34 ± 0.07 μm ($p \sim 1.0$)]. Thus, the regenerated hair bundles in the LES achieved heights by 70 d post-DT that were consistent with type II hair bundles in the LES of WT utricles.

As expected, the tallest stereocilia heights were much shorter for both WT-no DT type II hair cells and regenerated hair cells than for type I stereocilia, whether in WT-no DT mice or in surviving type I bundles in *DTR* mice (Fig. 4G). The surviving type I bundles had higher variance than the other bundles, so, to compare all bundles together, we also performed a Kruskal–Wallis ANOVA and *post hoc* Dunn's tests of significance. By this analysis, the surviving type I stereocilia heights did not differ significantly from the WT-no DT type I stereocilia and strengthen the evidence that the type I stereocilia were taller.

Nascent hair cells, like supporting cells, have apical microvilli. With time, the microvilli are replaced by stereocilia, specialized microvilli that are relatively thick and tall, with a staircase arrangement of heights. At maturity, the stereocilia of type II hair cells are thinner than those of type I hair cells (Rüsch et al., 1998). Figure 4H compares TEM measurements of the diameters of supporting cell microvilli and of type I and type II stereocilia from WT utricles with the diameters of regenerating *DTR* stereocilia at multiple times post-DT. These observations had homogeneous variance, and one-way ANOVA and *post hoc* Tukey's analysis showed that supporting cell microvilli were significantly thinner than all samples of hair cell stereocilia, both WT-no DT and regenerating, with the exception of the earliest regeneration time point, 28 d post-DT. The diameters of WT-no DT type I stereocilia significantly and substantially exceeded those of supporting cell microvilli and all other stereocilia, both WT type II and regenerating hair cells.

Thus, for regenerating hair cells in the LES, stereocilia started out thin, as they do in normal development, growing by 70 d post-DT to thicknesses and heights similar to those of WT-no DT type II stereocilia, but not of type I stereocilia. Wang et al. (2019) also noted relatively small bundles in regenerated hair cells in mouse utricles that were damaged during the neonatal period. Both our WT and *DTR* samples yielded smaller means and ranges of heights than Li et al. (2008) measured for type II
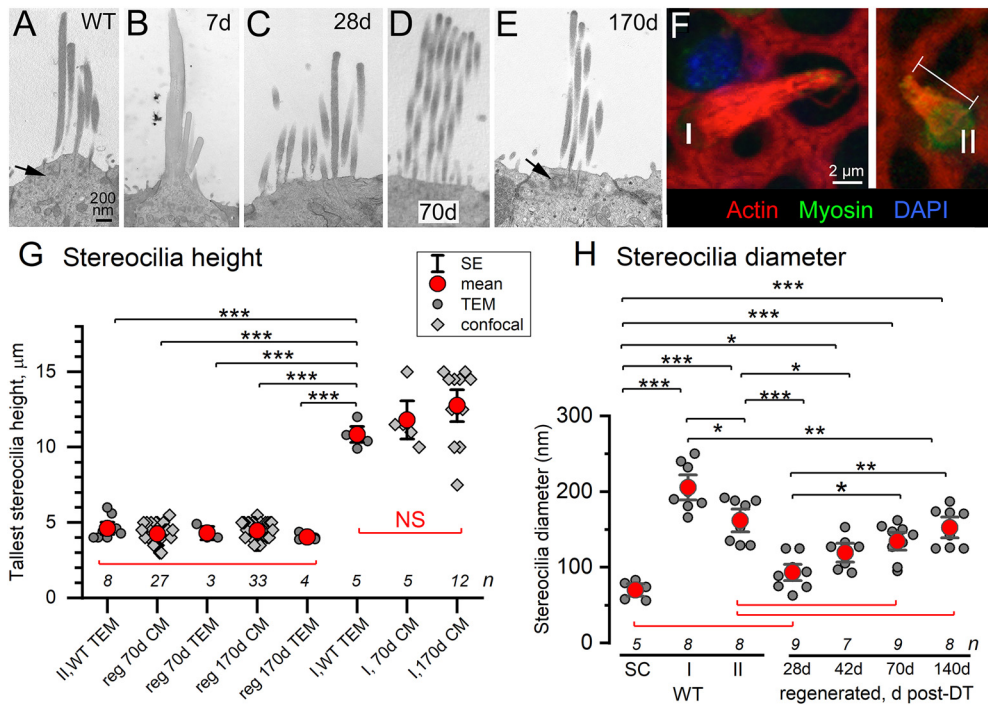
Figure 4. The stereocilia of regenerated hair cells grew over time post-DT to dimensions consistent with WT type II stereocilia. *A–E*, Hair bundles from a type II hair cell in a WT-no DT mouse (*A*) and regenerated *DTR* hair cells at increasing days post-DT (*B–E*). *A*, *E*, Arrows, cuticular plate. Scale bar: *A* (for *A–E*), 200 nm. *B*, Degenerating hair cell at 7 d post-DT had fused stereocilia. *C*, Newly regenerating hair cell at 28 d had immature stereocilia (short, thin stereocilia; no clear staircase of rows) implanted in a developing cuticular plate. *D*, *E*, Hair bundles of regenerated hair cells at 70 d (*D*) and 170 d (*E*) were longer; at 170 d, stereocilia diameter and staircase organization resembled WT-no DT bundles (*A*). *F*, Confocal micrographs of type I (left) and regenerated (right) bundles from a *DTR* mouse at 70 d post-DT. Phalloidin (red) labels actin in stereocilia and network of junctional complexes of supporting cells, DAPI (blue) labels cell nuclei, and myosin VIIa antibody labels hair cell cytoplasm and not supporting cells. Bar, Measured height of tallest stereocilia in a regenerated hair cell. *G*, Heights of tallest stereocilia were measured from TEM micrographs and/or confocal micrographs (CMs) for mature type II hair cells and type I hair cells in WT-no DT mice, versus regenerated hair cells or surviving type I hair cells from *DTR* mice at 70 and 170 d post-DT. Regenerated stereocilia in all conditions resembled WT-no DT type II stereocilia and were much shorter than type I stereocilia, whether WT-no DT or surviving type I stereocilia. *G*, *H*, *n* for group is given just above the *x*-axis; $*p < 0.05$, $**p < 0.001$, $***p < 0.0001$. Red brackets, NS comparisons. *H*, Stereocilia diameter was measured with TEM for regenerated hair cells at four times post-DT and compared with WT-no DT hair cells (types I and II) and supporting cell (SC) microvilli. SC microvilli were significantly thinner than all hair cell stereocilia except regenerating stereocilia at 28 d post-DT. Relative to WT type II stereocilia, regenerated stereocilia were thinner at 28 and 42 d post-DT and were not significantly different at 70 and 140 d post-DT. WT type I stereocilia were thicker than WT type II stereocilia and all regenerated stereocilia.

bundles in the LES of adult CD-1 mice (mean, 5.4 µm; range, ~3–10 µm). Possible factors in the difference include the following: (1) mouse strain: by electrical capacitance measures, CD-1 hair cells are larger than the hair cells in this study (A. González-Garrido, unpublished observations); and (2) method: the side-on confocal views obtained by Li et al. (2008) may have better captured the full range of hair bundle heights.

Regenerated hair cells transduced hair bundle deflections
Whole-cell mechanoelectrical transduction currents and receptor potentials were evoked by deflecting individual hair bundles with a rigid glass probe. The probe motion was aligned with the sensitive orientation axis of the hair bundle, and the probe was driven with a series of sinusoidal bursts at constant amplitude and incremented frequencies from 2 to 100 Hz. Transduction current (I_{met}) recorded from regenerated hair cells was compared with I_{met} from "control" hair cells, which were type II hair cells in utricles from C57BL/6J mice (the background strain for the *DTR* mice) that were not treated (no DT). Transduction currents and/or receptor potentials were detected in 14 of 38 (37%) regenerated hair cells tested and in 9 of 12 (75%) control hair cells tested.

Figure 5 shows examples of control (Fig. 5A.1–B) and DT-treated *DTR* (Fig. 5C.1–D) responses to the sinusoidal burst stimuli. Unlike anomalous responses reported in immature or damaged hair bundles (Beurg and Fettiplace, 2017), regenerated

hair cells had submicrometer operating ranges (Fig. 5E) and the normal response polarity: positive deflections, toward the tall edge of the hair bundle, evoked inward currents and depolarizing receptor potentials. In both control and regenerated hair cells, frequency dependence of the transduction current could be either flat (frequency independent; Fig. 5A.1,C.1) or high pass (rising with frequency; Fig. 5B,D), indicating variation across cells in the rate and/or extent of transducer adaptation (Songer and Eatock, 2013); transducer adaptation is more effective at low frequencies, causing the current to rise with stimulus frequency. Currents were usually measured at a holding potential of −64 mV, near the resting potential for type II hair cells. In the control data in Figure 5B, a more negative holding potential (−84 mV) increased the driving force on transduction current by ~30%.

For the exemplary control and *DTR* hair cells in Figure 5, *A* and *C*, we show both transduction currents (Fig. 5A.1,C.1) and receptor potentials recorded in current-clamp mode (Fig. 5A.2, C.2). Relative to I_{met}, receptor potentials showed additional frequency filtering by voltage-dependent properties, both active (voltage-gated ion channels) and passive (membrane charging time). For example, voltage-dependent properties transformed the flat frequency dependence of I_{met} in Fig. 5C.1 to bandpass tuning of the receptor potential of the same cell (Fig. 5C.2). The attenuation of the receptor potential at stimulus frequencies >20 Hz was reported previously for rodent utricular type II and
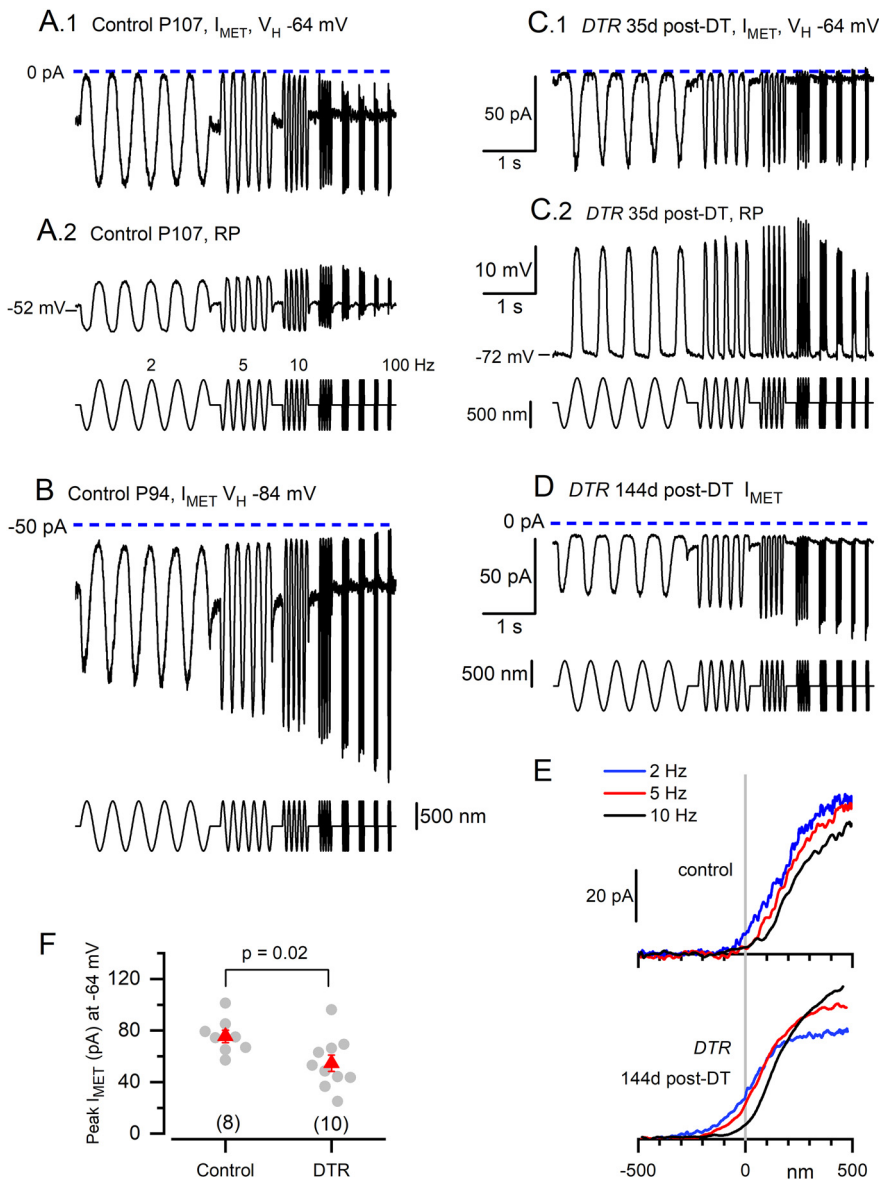
Figure 5. Regenerated hair cells transduced bundle deflections with smaller average maximum transduction currents than wild-type hair cells. ***A–D***, MET currents and receptor potentials were evoked by a series of sinusoidal hair bundle displacements (±500 nm, incremented from 2 to 100 Hz; stimulus shown below response traces). Averages of three to six sweeps. Data shown are from two control type II hair cells (C57BL/6J, no DT; ***A, B***) and two regenerated hair cells (***C, D***). Scale bars for DTR data in ***C.1, C.2***, and ***D*** apply to control data to the left (***A.1, A.2, B***, respectively). ***B, A.1, C.1, D***, The holding potential (V_H) values for voltage clamp were −64 mV (***A.1, C.1, D***) and −84 mV (***B***). ***A.2, C.2***, Zero holding current for current-clamp responses. ***E***, $I(X)$ relations generated from responses in ***D*** to positive-going half-cycles of the stimuli at 2, 5, and 10 Hz for control and DTR examples. ***F***, Average peak MET current (red symbols) was larger for control cells exceeded value (mean ± SEM) for the following: control cells, −76 ± 5 pA (n = 8; P94 to P107); versus regenerated DTR hair cells, −56 ± 6 pA (n = 10; 35–316 d post-DT; P95 to P377).

immature hair cells (Holt et al., 1999; Songer and Eatock, 2013), and reflects low-pass filtering set by the input resistance (R_{in}) and capacitance of the cells.

Figure 5E shows that the dependence of current on bundle displacement, the $I(X)$ relation, has the expected sigmoidal shape in both control and regenerated hair cells. As reported before for control hair cells, the operating range shifted toward more positive displacements as stimulus frequency increases (Songer and Eatock, 2013), possibly reflecting increasing intrastereociliary Ca^{2+}.

Figure 5F compares maximal peak–peak MET current amplitudes at the holding potential of –64 mV for 10 regenerated cells [35–316 d post-DT; postnatal day 95 (P95) to P377] and 8 control

cells (P94–P107, no DT) with stable transduction. The values from the regenerated cells overlapped those from control hair cells, but the average was 35% smaller (mean ± SEM: −56 ± 6 pA vs. −76 ± 5 pA (control); p = 0.023, one-way ANOVA and Tukey's means test; effect size (Cohen's d) 1.2). There was no trend toward larger currents with more time available for regeneration (linear regression slope, –0.117 ± 0.9 pA/d post-DT; r^2 = 0.17). The comparatively small transduction currents of regenerated hair cells were capable of producing large receptor potentials, as illustrated in Fig. 5C.2, because regenerated hair cells often had high-input resistances (>1 GΩ; see below). No difference was detected in the maximum receptor potentials of control and DTR cells [control cells, 19.6 ± 3.2 mV (n = 6); DTR cells, 23.6 ± 3.0 mV (n = 6; p = 0.38)].

For both control and regenerated hair cells, the mean values of I_{met} are smaller than reported for neonatal hair cells from the utricles of CD1 mice (150–170 pA; Géléoc et al., 1997; Holt et al., 1997; Géléoc and Holt, 2003; Vollrath and Eatock, 2003). This difference may reflect differences in mouse strains and ages: the advanced age of both control and DTR preparations relative to reported CD1 data may have reduced I_{met} in vivo and/or made I_{met} more susceptible to damage during preparation for in vitro experiments. As control C57BL/6J mice age beyond 6 months, I_{met} in cochlear hair cells decreases, which may contribute to the observed increase in Auditory Brainstem Response (ABR) thresholds (Jeng et al., 2021). However, vestibular evoked potentials, thought to be a sign of striolar (S) function in otolith organs, show much less deterioration with age in C57BL/6J mice (Mock et al., 2016).

In summary, I_{met} values of DTR hair cells are smaller than those of C57BL/6J type II hair cells, suggesting that the regenerated hair cells are more fragile, or less differentiated, or represent a subpopulation of the normal set of mature type II hair cells. Each of these possibilities could contribute to the lack of restoration of balance to the whole animal.

Voltage-dependent properties of regenerated hair cells were type II like

The mechanoelectrical transduction current of the hair cell changes membrane voltage, modulating voltage-sensitive basolateral currents that contribute to shaping the receptor potential and mediate release of transmitter. In altricial rodents (mice, rats, and gerbils), hair cells change ion channel expression significantly during the period between birth and the opening of eyes
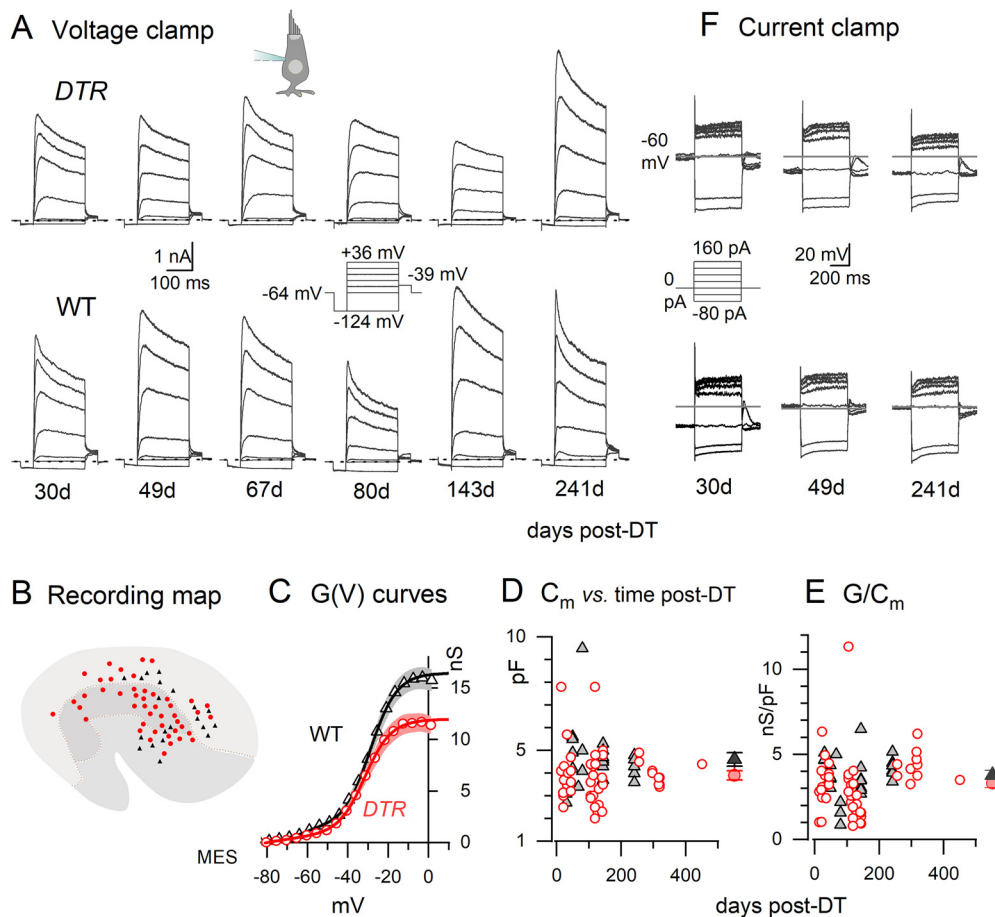
Figure 6. Regenerated *DTR* hair cells and WT type II hair cells shared key electrophysiological properties. *A*, Exemplar voltage-dependent current families from *DTR* (top) and WT (bottom) utricular maculae, at increasing days post-DT (left to right). Voltage-clamp protocol (middle, aligned with 80 d post-DT data) applies to all. Dashed lines, 0 nA; holding potential, −64 mV. All *DTR* cells are shown except the one at ∼70 d post-dT, which had basolateral processes (cartoon). *B*, Sites of recorded hair cells on the utricular macula, located by aligning photomicrographs of the fluorescently labeled hair cell with a standard map of the utricle (based on the images in Figures 1–3 in Li et al., 2008). Utricular zones are as follows: top to bottom: lateral extrastriola (light gray), striola (gray), medial extrastriola (medium gray). Black triangles, WT; red circles, *DTR*. *C*, G(V) curves fitted to averaged tail current data at −39 mV from 48 *DTR* and 24 WT cells (Eq. 1) had similar voltage dependence but smaller mean conductance values. Shaded areas, Mean values ± SE. Fits (Eq. 1): *DTR*: $G_{max} = 12.3 \pm 0.2$ nS; $V_{1/2} = -32.3 \pm 0.4$ mV; $S = 7.9 \pm 0.3$ mV; WT: $G_{max} = 17.3 \pm 0.4$ nS; $V_{1/2} = -29.8 \pm 0.7$ mV; $S = 8.8 \pm 0.5$ mV. *D*, Membrane capacitance (proportional to surface area) as a function of days post-DT. *DTR* cells (red circles) were smaller on average than WT cells (gray triangles). Filled symbols to the right in *D* and *E* are the mean ± SE. *E*, Conductance density (in nanosiemens per picofarad) was similar for *DTR* and WT cells across time post-dT. *F*, Exemplar families of voltage responses to injected currents from several of the cell pairs shown in *A*. *DTR* cells are at top; WT cells are below. Current-clamp protocol (middle, aligned with 30 d post-DT data) applies to all.

and the middle ear at ∼P12 (for review, see Eatock and Hurley, 2003; Goodyear et al., 2006). In addition to the transduction channels of the apical hair bundle (above), rodent vestibular hair cells acquire, as they mature, basolateral channels of several varieties: outwardly rectifying potassium (K⁺)-selective channels and HCN channels, and inwardly rectifying K⁺-selective (K$_{IR}$) channels. Voltage-gated calcium and Na$_V$ channels are added and then pruned in the early postnatal period, so that their expression peaks while synapses are forming.

There are qualitative and quantitative differences between hair cell types in the specific ion channels that are expressed and the detailed time course of expression during differentiation. One of the most striking differences between mature type I and type II vestibular hair cells is that only type I cells express a large K⁺ conductance ($g_{K,L}$) that is significantly activated at resting potential (Correia and Lang, 1990), affecting the gain and time course of the receptor potential (Rennie et al., 1996; Songer and Eatock, 2013) and mediating an unusual form of synaptic transmission with the afferent calyx ending (Contini et al., 2017). We have therefore used voltage-dependent membrane conductances as an indicator of the functional differentiation of the

regenerated hair cells from *DTR* mice. We recorded whole-cell voltage-sensitive currents and voltage responses to current steps from 48 regenerated hair cells and 24 control type II hair cells from 22 *DTR* and 6 WT littermates treated with DT. With the goal of capturing any delayed regeneration, we recorded from a broad range of post-DT times, as follows: 14–451 d post-DT (median, 119 d) for the *DTR* sample; and 30–241 d post-DT (median, 143 d) for the WT littermates. The ranges of postnatal ages were as follows: *DTR*, 86–541 d (median, 186 d); WT, 102–274 d (median, 185 d). In both *DTR* and WT animals, we sampled cells from three recognized zones of the sensory epithelium (S, LES, and MES; Fig. 6A).

Morphology of recorded cells
With differential interference contrast and fluorescence microscopy of semi-intact DT-treated epithelia, the regenerated hair cells of *DTR* mice after 70 d post-DT appeared to be type II rather than type I, based on their basolateral processes and lack of calyces (Fig. 1), relatively small hair bundles (Fig. 4), and expression of hair-cell specific voltage-gated conductance (below). We also saw a small number of type I hair cells, which,

based on morphologic studies, survived the DT treatment. Most if not all of the type II hair cells we recorded from in *DTR* mice were regenerated, rather than retained, because DT kills 90–95% of hair cells in the macula within 14 d (Golub et al., 2012).

During whole-cell recording, a fluorescent dye (sulforhodamine 101) in the recording solution diffused into the cell, allowing visualization of cell shape with fluorescence optics in most cases. Basolateral processes were evident in ~80% of the regenerated hair cells scattered throughout the epithelium (38 of 48 cells; Fig. 6B, red symbols), and in ~50% of the WT type II hair cells from littermate controls (10 of 19 cells with documented morphology; not shown in Fig. 6). This is lower than the percentage for type II hair cells in microscopic studies of fixed adult mouse utricles (~80%; Pujol et al., 2014), possibly indicating that basolateral processes were sometimes resorbed during whole-cell recording. In CD-1 mice (A. González-Garrido, unpublished observations) and in the current sample of *DTR* mice, the presence of basolateral processes did not correlate with any electrophysiological feature that we studied, including input resistance, capacitance, and properties of the dominant outwardly rectifying current. Therefore, we have pooled electrophysiological observations from regenerated cells with and without basolateral processes.

Mean resting potentials and input resistances of hair cells from *DTR* and WT mice did not differ significantly [–61 ± 2.3 mV (48 *DTR* cells) vs –66 ± 1.8 mV (24 WT cells; $p = 0.3$); and 1.33 ± 0.19 GΩ (*DTR*) vs 1.02 ± 0.21 GΩ (WT, $p = 0.4$)]. These values are in the range previously reported for type II hair cells from rodent vestibular epithelia and for immature hair cells that were not identified as type I or type II (Rüsch et al., 1998). Differentiated type I hair cells in contrast have more negative resting potentials (–70 to –80 mV) and much lower input resistances (<200 MΩ), reflecting the effects of a large resting K$^+$-selective conductance, $g_{K,L}$.

Basolateral voltage-dependent conductance

Figure 6A compares voltage-dependent current families in exemplar regenerated (*DTR*) hair cells and type II hair cells from DT-treated WT littermates, with time relative to DT treatment increasing from left to right. In both genotypes, the current families are dominated by large outward (positive) currents evoked by depolarizations positive to the holding potential of –64 mV (near average resting potential, above), with grossly similar time courses and voltage dependence of activation. In no case did a regenerated hair cell express $g_{K,L}$, a hallmark of mature type I cells that is readily apparent in such current families (See Fig. 11B).

To quantify the voltage dependence of outward currents, we generated activation curves of conductance versus voltage for our samples of WT type II and *DTR* regenerated hair cells, as described in Materials and Methods. The resulting mean activation curves (Fig. 6C) have strongly overlapping voltage dependence. *DTR* hair cells had a smaller average G_{max} [12.5 ± 1.0 nS ($n = 48$) vs 16.4 ± 1.0 nS ($n = 24$), $p = 0.01$; effect size (Cohen's d), 0.68]. Comparison of surface areas of the two populations show that the smaller conductance of the *DTR* cells can be accounted for by their smaller average surface area. Figure 6D shows membrane capacitance (C_m), which is proportional to surface area, as a function of time post-DT for both samples (range, 14–451 d post-DT). The mean values differed significantly: 3.9 ± 0.2 pF (*DTR*, $n = 48$) versus 4.6 ± 0.3 pF (WT, $n = 24$; $p = 0.02$; Cohen's d, 0.56), and the regenerated hair cells did not get larger with time post-DT (linear regression of *DTR* data:

slope, –2.5E-4 ± 0.002 pF/d; adjusted R^2 value, –0.02). Normalizing G_{max} by C_m for each hair cell (Fig. 6E) yielded similar mean conductance densities: 3.8 ± 0.25 nS/pF (WT) and 3.3 ± 0.26 nS/pF (*DTR*; $p = 0.2$, Welch's correction) and therefore similar numbers of outwardly rectifying K channels per square micrometer. Similarly, WT and *DTR* voltage responses to iterated current steps did not clearly differ, as illustrated in Figure 6F.

Closer inspection, however, reveals differences between WT and *DTR* regenerated cells in the expression of the voltage-sensitive HCN current (I_h) and Na$_V$ current (I_{Na}). As shown previously for type II hair cells from CD-1 mouse utricles (Rüsch et al., 1998; Horwitz et al., 2011) and other vestibular organs, hyperpolarizing voltage steps activate I_{IR} (current through fast inwardly rectifying K$^+$-selective channels) and I_h (current through slowly activating HCN channels, which are permeable to both K$^+$ and Na$^+$). K$_{IR}$ channels are present throughout the postnatal period, but HCN channels (mostly HCN1; Horwitz et al., 2011) are acquired by maturing type I and type II cells in mice between P3 and P8 (Rüsch et al., 1998; Géléoc et al., 2004), overlapping with the addition of $g_{K,L}$ channels to type I cells. As expected, at times >100 d post-DT, WT type II hair cells consistently expressed both I_{IR} and I_h (Fig. 7A). Regenerated hair cells expressed I_{IR} consistently and at similar density (per membrane area) to WT cells. In contrast, I_h was expressed in fewer regenerated cells (21 of 48 cells) and when present had significantly lower conductance density (Fig. 7A): 80 ± 12 pS/pF (*DTR*, $n = 21$) versus 205 ± 18 pS/pF (WT, $n = 21$; $p < 10^{-6}$). Conductance was calculated from current, measured as shown in Figure 7A.1, and assuming a reversal potential of –44 mV (Rüsch et al., 1998).

In the rat utricle, nearly all neonatal hair cells express transient Na$_V$ currents (Lennan et al., 1999; Chabbert et al., 2003), which take two forms ($I_{Na,1}$, $I_{Na,2}$) with quite different voltage dependence (Wooltorton et al., 2007). Most notably, the voltage range of inactivation was ~15 mV more negative for $I_{Na,1}$ than for $I_{Na,2}$. The incidence of both currents drops substantially by P7, with no hair cells expressing the less negative conductance ($I_{Na,2}$) by P10. In older rat utricles (Brugeaud et al., 2007) denervation can cause the expression of Na$_V$ current in hair cells. In our recordings, no I_{Na} was detected in any DT-treated WT type II hair cells (0 of 24 cells). In contrast, 25 of 48 of regenerated *DTR* hair cells (~50%) expressed either $I_{Na,1}$ or $I_{Na,2}$ (Fig. 7B.1–B.4). Regenerated hair cells with I_{Na} were recorded in different epithelial zones (data not shown) and out to many days post-DT (range, 14–451 d post-DT; Fig. 7B.5).

To summarize the results from whole-cell recordings of voltage-gated currents, regenerated hair cells from different zones in DT-treated epithelia did not manifest clear zonal differences in passive properties [resting potential, C_m, or R_{in}] or in the expression of voltage-sensitive conductances. They had a smaller average surface area than WT hair cells from DT-treated utricles, as indicated by C_m measurements, which may reflect in part the absence of large hair bundles in the regenerated population. No regenerated hair cells expressed the low-voltage-activated $g_{K,L}$ typical of mature type I hair cells, nor were any innervated by afferent calyces. In CD-1 mouse utricles, type I hair cells acquire both calyces and $g_{K,L}$ beginning at E18 (Géléoc et al., 2004) and extending through the first postnatal week (Rüsch et al., 1998; Géléoc et al., 2004). Calyces do not appear to be required for $g_{K,L}$, which appears with a similar time course in denervated, cultured utricles as *in vivo* (Rüsch et al., 1998). The outwardly rectifying voltage-sensitive channels of regenerated hair cells instead resembled those of mature type II hair cells in their time course and voltage
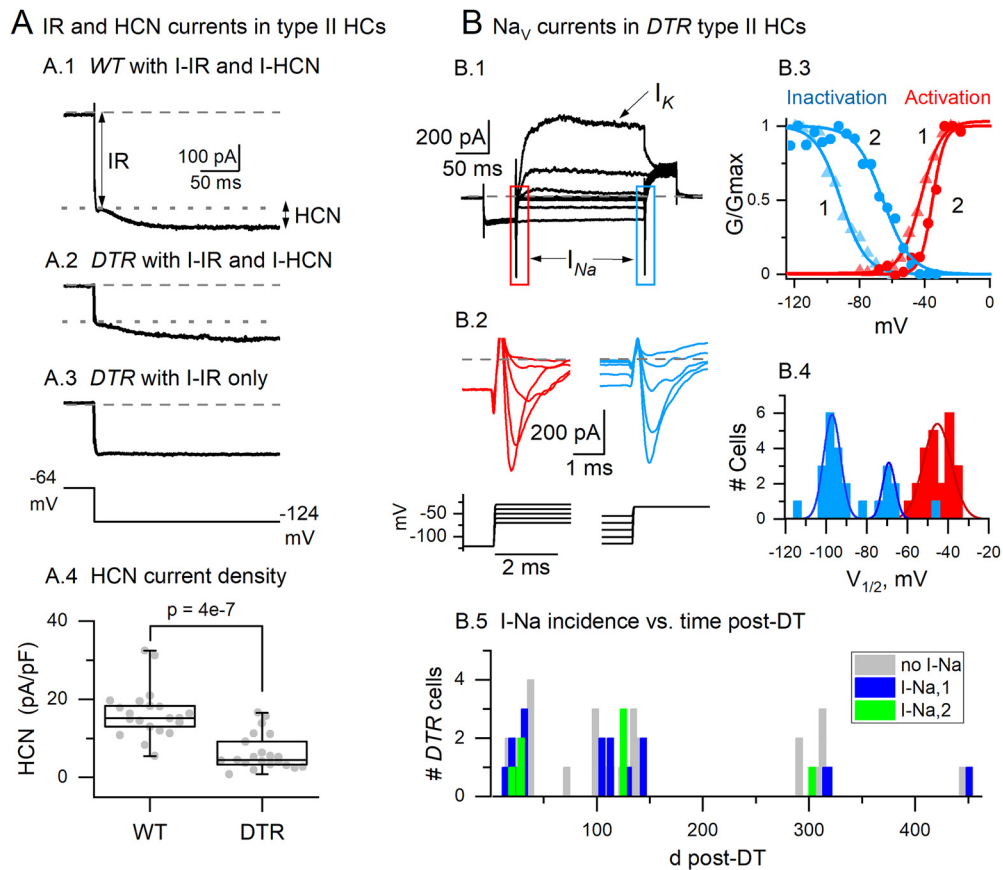
Figure 7. Regenerated *DTR* hair cells differed from adult WT type II hair cells (HCs) in average expression of Na$_V$ and HCN voltage-dependent currents. ***A***, Hyperpolarizing voltage steps evoked both I_{IR} and I_{HCN} in WT (***A.1***) and some regenerated *DTR* cells (***A.2***), but not in all (***A.3***). ***A.4***, *DTR* cells with I_{HCN} had smaller current density than WT (box plot shows median, 25–75% range, minimum, and maximum; red triangles, mean values). ***B.1***, Voltage-clamp recordings from many *DTR* hair cells revealed voltage-gated I_{Na} for depolarizing steps from a negative prepulse (boxes). ***B.2***, Expanded boxed areas in ***B.1*** showing transient I_{Na} at the beginning and end of iterated test step. ***B.3***, Activation and inactivation curves for I_{Na}, fitted with Boltzmann Equation 1. ***B.4***, Distributions of activation and inactivation midpoints ($V_{1/2}$ values; Eq. 1); the inactivation distribution (blue) is bimodal, consistent with Na$_V$ conductance in $I_{Na,1}$ and $I_{Na,2}$. ***B.5***, Some regenerated *DTR* hair cells expressed $I_{Na,1}$ or $I_{Na,2}$ long after DT treatment. At all ages shown, no WT hair cells expressed I_{Na}.

dependence, activating positive to resting potential. As a consequence, the regenerated hair cells had high R$_{in}$, in excess of >1 GΩ, and resting potentials typical of type II hair cells and significantly less negative than those of type I cells.

The voltage-sensitive basolateral conductances of regenerated *DTR* hair cells did differ from those of WT type II counterparts in several of the following ways: (1) HCN channels are acquired postnatally and are uniformly reported in mature WT utricular hair cells, including in this study, but were detected less often in the regenerated cells and were at lower density when present; and (2) Na$_V$ conductance was not detected in any WT cells but was present in approximately half of the regenerated cells, with the two ranges of voltage dependence previously reported in immature rodent hair cells. With respect to HCN and Na$_V$ channel expression, therefore, some of the regenerated cells resembled immature hair cells in normal rodent utricles.

Regenerated hair cells formed ribbon synapses with vestibular afferents

We examined synapses made by regenerated type II hair cells on vestibular afferent fibers with transmission electron and confocal microscopy. After 28 d post-DT, the majority of regenerated hair cells had mature-appearing afferent synapses. Figure 8A shows a classical ribbon synapse between the basolateral process of a type II hair cell and an afferent bouton in a WT mouse at 42 d post-DT. This synapse included a presynaptic compartment with a ribbon

surrounded by synaptic vesicles (arrows), including some positioned against the presynaptic membrane. On the postsynaptic side, the bouton had sparse cytoplasm with mitochondria and few vesicles, and a well formed membrane thickening (arrowhead) that represents the site of glutamate receptors. Figure 8, *B* and *C*, show examples in regenerated *DTR* hair cells of mature ribbon synapses, also between the basolateral processes of the hair cell and the afferent bouton. In their ultrastructure, both the bouton and the ribbon synapse resemble their WT counterparts in every respect.

We quantitatively assessed synapses by labeling utricles from WT and *DTR* mice with antibodies to the following: myosin VIIa, a hair cell marker; Ctbp2, a protein enriched in the presynaptic ribbon (Schug et al., 2006; Uthaiah and Hudspeth, 2010); and GluA2, an AMPA-type glutamate receptor postsynaptic to ribbons in the afferent membrane (Pujol et al., 2014; Sadeghi et al., 2014; Fig. 8D–H). We took high-magnification *z*-stack images of several WT type II and regenerated hair cells at the level of their basolateral processes (marked by myosin VIIa immunoreactivity; Fig. 8I), where ribbon density is highest (Pujol et al., 2014). At 170 d post-DT treatment, the percentage of Ctbp2$^+$ particles (presynaptic ribbons) that colocalized with GluA2$^+$ particles (postsynaptic receptors) was ~85% for *DTR* mice and WT mice (Fig. 8J). Results are similar for both WT mice that received DT treatment and WT mice that did not (Fig. 8J), indicating a lower Ctbp2 and GluA2 colocalization than the ~100% colocalization in the rat cochlea (Martinez-Monedero et al.,
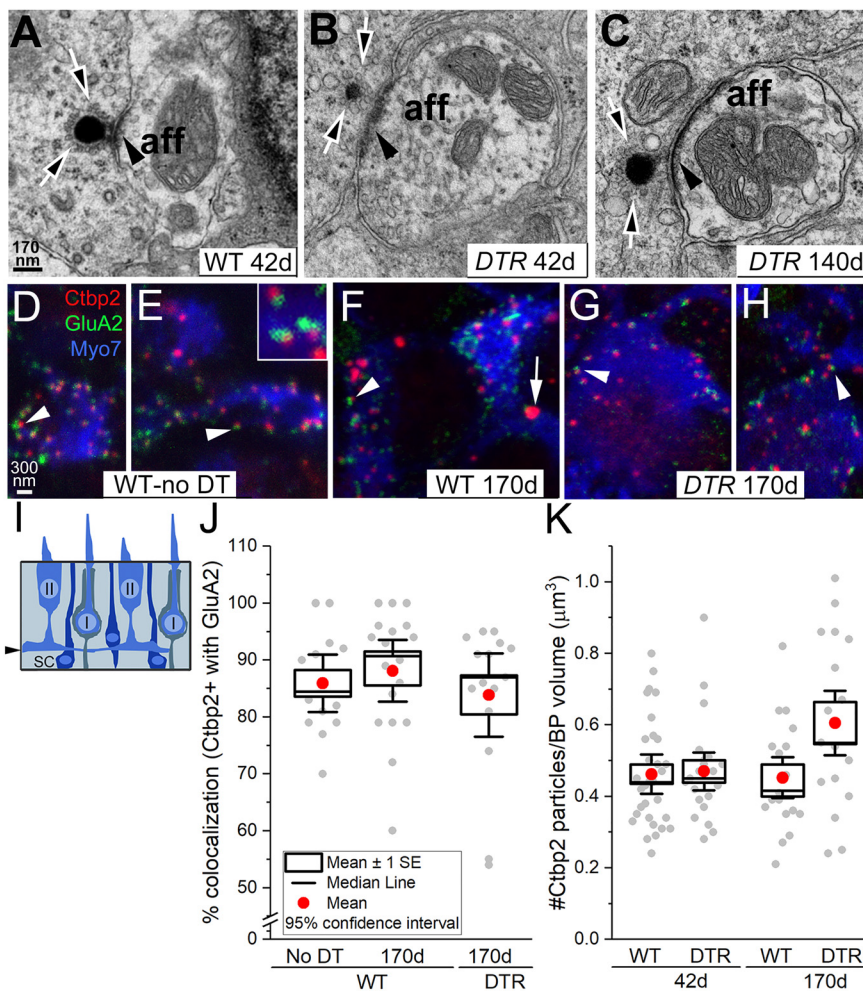
Figure 8. Synapses formed between regenerated *DTR* hair cells and afferent nerve terminals. *A–C*. Transmission electron micrographs of ribbon synapses between HCs and afferent boutons. *A*, A normal type II hair cell from a WT mouse at 42 d post-DT. *B*, *C*, A regenerated hair cell from a *DTR* mouse at 42 d post-DT (*B*), and a regenerated hair cell from a *DTR* mouse at 140 d post-DT (*C*). Different apparent sizes of ribbons may in part reflect slices through their edges versus centers. Note similarity of the ultrastructure: arrows, ribbons surrounded by neurotransmitter vesicles; arrowheads, postsynaptic densities in the afferent bouton. Scale bar: *A* (for *A–C*), 170 nm. *D–I*, Confocal slices through WT and WT-no DT type II hair cells and regenerated *DTR* hair cells at long times post-DT; slices were at the basolateral process level, as schematized in *I* (arrow). Arrowheads, Colocalized Ctbp2 and GluA2 labeling. *Scale bar*: *D* (for *D–H*), 300 nm. *E*, Inset, co-localization of Ctbp2 and GluA2 at high magnification. *F*, Arrow, large Ctbp2-positive particle in a type I hair cell. *J*, Percentage of Ctbp2$^+$ particles that colocalize with GluA2, for 32 WT cells (WT-no DT cells, 14; WT cells, 18) and 15 *DTR* cells at 170 d post-DT. One to three basolateral processes were sampled per cell. *K*, Density of Ctpb2 particles in basolateral processes of the same cells as in *J*.

2016). We also examined the density of Ctbp2$^+$ ribbons in the basolateral processes of WT and *DTR* mice at 42 and 170 d post-DT (number of ribbons per volume of process measured; Fig. 8*K*). Two-way ANOVA found no effect of genotype (WT vs *DTR*, $p = 0.24$) or time post-DT ($p = 0.18$) on ribbon density. Collectively, these findings indicate that many afferent synapses acquire mature synaptic features.

Distributions of ribbon precursors and mature ribbons in regenerated hair cells became more normal with time post-DT

With transmission electron microscopy, we observed signs of immaturity in the ribbon synapses of regenerated hair cells. Although less frequently, some apparently immature ribbon synapses were also found in normal (WT) type II hair cells, indicative of ongoing plasticity of ribbon synapses, especially at the level of basolateral processes.

Compared with WT, most regenerated hair cells, up to 2 months post-DT, had an increased number of ribbons in immature form: ribbon precursors, ectopic ribbons, and complex (multiple) ribbons. Ribbon precursors are considered to be an early step in the assembly of ribbon synapses and have been described in developing retinal photoreceptors (Regus-Leidig et al., 2009) and in hair cells of developing or regenerating zebrafish neuromasts (Suli et al., 2016). Ectopic ribbons were first described in the developing mouse cochlea (Sobkowicz et al., 1982) and in guinea pig hair cells after excitotoxic injury to afferents (Puel et al., 1995; Ruel et al., 2007). Complexes of multiple adjacent ribbons have been described in developing cochlear hair cells of rodents (Lenoir et al., 1980; Sobkowicz et al., 1982).

In both WT-no DT hair cells and regenerating hair cells in this study, ribbon precursors had the electron-dense core of the ribbon but lacked associated synaptic vesicles (Fig. 9*A–E*). They were encased in a tubular or vesicular membrane-bound structure resembling smooth endoplasmic reticulum (Fig. 9*B,C,D',E'*). They were often located away from the external plasma membrane, sometimes above or at the level of the cell nucleus. Ribbon precursors appeared to migrate basally to the synaptic pole, where their electron-dense core becomes surrounded by microvesicles. Even when ribbons were surrounded by synaptic vesicles and no longer inside endoplasmic reticulum, they sometimes showed other signs associated with immaturity, including complexes of multiple aligned ribbons (Fig. 9*F*) and ectopic locations (Fig. 9*G*).

Based on electron micrographs, we quantified ribbons that were in a precursor state or were mature (located at the membrane, surrounded by vesicles, and juxtaposed to a postsynaptic density on a bouton) in WT mice and in mice at various stages of regeneration. The number of ribbon precursors per hair cell changed significantly at short times after DT treatment (one-way ANOVA, $p = 0.015$). Ribbon precursor numbers were higher in regenerated hair cells at 28–42 d post-DT relative to WT type II hair cells, but were similar to WT cells at 140–170 d post-DT (Tukey's multiple-comparisons test; Fig. 9*I*). The number of mature synapses was significantly reduced in *DTR* mice at 28–42 d post-DT relative to WT mice (one-way ANOVA, $p = 0.022$) with partial recovery by 140–170 d post-DT (Fig. 9*J*). Thus, ribbon synapses formed on regenerated hair cells ~28–42 d post-DT and became more mature by 140–170 d post-DT, consistent with our observation that there was no difference in colocalization of presynaptic and postsynaptic proteins between WT type II controls and *DTR* regenerated hair cells at 170 d post-DT.

Most postsynaptic afferent contacts with regenerated hair cells were mature-appearing boutons by 42 d post-DT, as indicated by numerous mitochondria, microtubules, and microfilaments, and few vesicles (Fig. 8A–C). However, as late as 170 d post-DT, we saw some boutons that appeared smaller and were filled with vesicles of various sizes and electron densities (Fig. 9H). This form of bouton is characteristic of a developing (Lenoir et al., 1980) or regrowing (Puel et al., 1995) inner ear afferent. Immature-appearing boutons were most frequent at early stages of regeneration (28-42 d post-DT) but were also seen occasionally in WT mice, particularly on basolateral processes (data not shown). Our observations suggest that afferent boutons on regenerated hair cells grow to more closely resemble normal boutons over time and that both normal mature hair cells and late-stage regenerated hair cells are occasionally contacted by immature-appearing boutons.

Regenerated hair cells received efferent inputs
Efferent neurons made synapses with similar ultrastructure on WT-no DT type II hair cells (Fig. 10A) and regenerated hair cells at 100 d post-DT (Fig. 10B) and other times. The presynaptic efferent nerve terminal was filled with small, clear, and uniformly sized vesicles (arrows), forming a cluster next to the hair cell membrane. On the hair cell side, the classical postsynaptic cistern was visible (Fig. 10A,B, arrowheads). Axodendritic synapses were seen between efferent varicosities and afferent neurites at 28 d post-DT (Fig. 10C) and later.

In summary, regenerated hair cells made normal afferent and efferent synapses. Up to 42 d post-DT, many ribbon synapses were immature, but beyond 42 d post-DT, most had a mature appearance.

Some surviving type I hair cells and postsynaptic calyces had normal morphology and electrophysiology
We detected occasional hair cells with features typical of type I hair cells (flask shape, surrounded by a normal-appearing calyx, ribbon synapses) in DTR utricles at a variety of times post-DT; Figure 11A shows examples at 28 and 140 d post-DT. Based on previous studies (Bucks et al., 2017; Hicks et al., 2020), these cells did not derive from supporting cells, but rather represented rare survivors of DT treatment. Some of these surviving type I hair cells had a healthy appearance, with normal cytoplasm and nucleus, and healthy calyces (Fig. 11A, arrows, top and bottom panels). Other surviving type I hair cells showed signs of cytolytic degeneration, such as highly vacuolated cytoplasm devoid of organelles (Fig. 11A, arrowhead) or apoptosis (Fig. 1H). We recorded whole-cell voltage-gated currents from several healthy-appearing surviving type I hair cells (Fig. 11B) and their afferent calyces (Fig. 11C) in DTR utricles and found them normal.
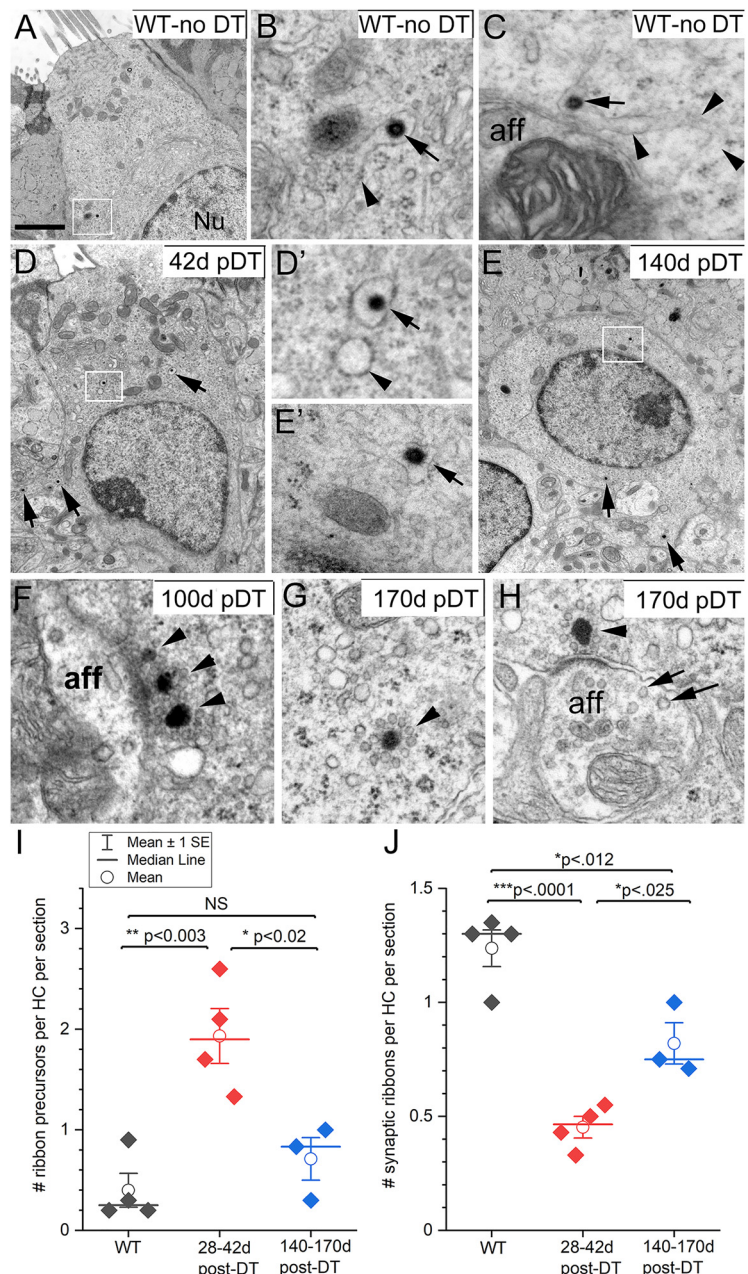

Figure 9. Distributions of ribbon precursors and ribbon synapses became more normal in regenerated DTR hair cells with time. **A–H**, TEM of ribbon structures in mature WT-no DT type II hair cells (**A–C**) and regenerated hair cells from DTR mice at different times post-DT (**D–H**). **A–C**, Ribbon precursors in mature WT hair cells. **A, B**, Ribbon precursor in box in **A** is magnified in **B** (arrow). **B**, Arrowhead, Tubular membrane containing the precursor. Nu, Nucleus. **C**, Another ribbon precursor (arrow) in endoplasmic reticulum (arrowheads) near a bouton afferent (aff). **D, E**, Similar ribbon precursors in regenerated DTR hair cells; boxed areas are magnified in **D′** and **E′**. **F**, Synapse with multiple ribbons (arrowheads) facing an afferent bouton. **G**, Ectopic ribbon surrounded by synaptic vesicles (arrowhead). **H**, Ribbon synapse with a single ribbon (arrowhead) contacting an immature-appearing afferent bouton with vesicles of different sizes (arrows). **I, J**, Numbers of ribbon precursors (**I**) or ribbons at synapses (mature ribbons; **J**) per basolateral process per section, compared between WT-no DT mice and DTR mice at short and long times post-DT. Scale bar: **A** (for **A, D, E**), 2 μm; **A** (for **B, C, D′, E′, F–H**), 350 nm.

The voltage-dependent hair cell currents were dominated by the type I-specific low-voltage K^+ conductance (i.e., $g_{K,L}$). The voltage protocol used (Fig. 11B.1) is designed to first close $g_{K,L}$ channels that are open at resting potential by stepping the voltage negative to their activation range, and then to reopen them with iterated depolarizing steps that activate them, as shown in the activation curve of Figure 11B.2. The midpoints of the curves
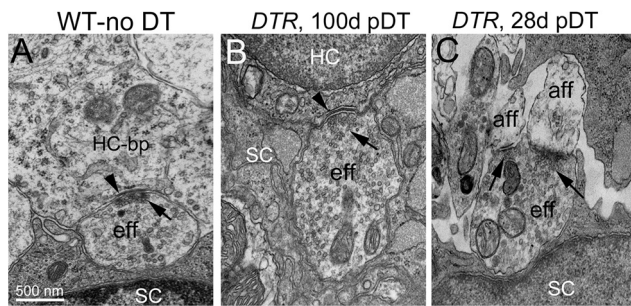
Figure 10. Efferent varicosities made normal synapses on regenerated *DTR* hair cells. ***A***–***C***, TEM micrographs of efferent synapses in WT-no DT (***A***) and *DTR* (***B***, ***C***) utricles at different times post-DT. Arrows in all panels point to clusters of presynaptic vesicles at efferent synapses. ***A***, Efferent varicosity (eff) contacts the basolateral process (bp) of a type II hair cell and a supporting cell, labeled SC in its nucleus. Note the numerous uniform vesicles throughout the axoplasm of the presynaptic efferent varicosity. Arrowhead, Postsynaptic cistern in hair cell, facing efferent synaptic vesicles (arrow). ***B***, Efferent varicosity forming a synapse on a regenerating hair cell; in all features, the varicosity and synapse appear similar to WT. ***C***, Efferent varicosity forming axodendritic synapses (arrows) on two afferent neurites (aff). The other side of the varicosity is in close contact with a supporting cell. Scale bar: ***A*** (for ***A***–***C***), 500 nm.

(Eq. 1, $V_{1/2}$ values; in Materials and Methods) are ~40–50 mV negative to the midpoints of the dominant outwardly rectifying K^+ currents in type II cells (Fig. 6C). This striking difference is consistent with literature on mature type I and type II hair cells in diverse amniotes, including birds, where the distinction was first noted (Correia and Lang, 1990); reptiles (Brichta et al., 2002); and mammals (Rennie and Correia, 1994; Rüsch and Eatock, 1996).

Figure 11C shows examples of normal physiology recorded from calyces that were postsynaptic to surviving type I hair cells in *DTR* utricles. By comparison with previous reports from rat saccule (Songer and Eatock, 2013) and mouse utricle (Horwitz et al., 2014; Ono et al., 2020), the calyces had normal complements of Na$_V$, HCN, and outward K^+ currents (Fig. 11C.1). Two examples of spontaneous spiking (Fig. 11C.2) illustrate the variation in spike timing regularity typical of vestibular afferents (for review, see Goldberg, 2000).

In summary, type I hair cells that survive DT treatment can retain physiological function and morphologic contact with afferent calyces. It is not surprising that they do not sustain vestibular function in the animal, given that surviving type I hair cells represent ~5% of the original population (Golub et al., 2012).

Discussion

Our previous studies (Golub et al., 2012; Bucks et al., 2017; Hicks et al., 2020) showed that DT-mediated hair cell destruction in adult mouse utricles stimulates supporting cells to transdifferentiate to hair cells that appear type II like in gross morphology, including the absence of afferent calyceal endings. Here, we set out to determine whether absent or deficient hair cell function could account for the lack of balance restoration and to document the extent of transdifferentiation possible with a long regeneration period. Regenerated hair cells acquired several morphologic, molecular, and physiological features typical of normal type II hair cells, but immature physiological properties were evident in some hair cells even months after DT. We also found no evidence for the emergence of type I properties: no developing afferent calyces, no $g_{K,L}$, and no large hair bundles. These differences may contribute to the persistence of overt symptoms of vestibular dysfunction (poor postural control, head bobbing, and body spinning) despite significant regeneration of hair cells.

Ribbon synapses of type II hair cells in normal adult mouse utricles

We made new observations in normal type II hair cells in adult mice. First, ~15% of Ctbp2-marked synaptic ribbons were not juxtaposed to GluA2-labeled postsynaptic elements. In rat crista, Sadeghi et al. (2014) also noted that Ctbp2-marked ribbons were less colocalized with GluA2 receptor patches than those of cochlear inner hair cells. However, our finding contrasts with inner hair cells from the adult rat cochlea, in which nearly 100% of ribbons colocalize with a postsynaptic element (Martinez-Monedero et al., 2016). In addition, some normal adult type II hair cells had ribbon precursors consisting of an electron-dense core without associated synaptic vesicles, sometimes located far from the plasma membrane, as observed in the developing mammalian cochlea (Lenoir et al., 1980). Similar ribbon precursors were observed in regenerationg hair cells from zebrafish lateral line (Suli et al., 2016). Because unapposed ribbons occurred in many normal type II hair cells, it is unlikely that they are restricted to the small number of immature type II hair cells arising through spontaneous hair cell turnover in adult mouse utricles (Forge et al., 1993; Lambert et al., 1997; Bucks et al., 2017). Rather, we infer that ribbon synapses in mature type II hair cells may undergo remodeling in normal conditions.

Regenerated hair cells in adult mouse utricles acquired ultrastructural and electrophysiological properties of type II cells

In adult rodents, vestibular hair cells that are replaced naturally after damage have type II-like gross morphology, whether damage is caused by DT (Golub et al., 2012), aminoglycoside antibiotics (Forge et al., 1993; 1998; Kawamoto et al., 2009), or 3,3′-iminodipropionitrile (Sayyid et al., 2019). For example, in the mouse utricle after DT-mediated damage, hair cells that have tall stereocilia and calyces typical of type I hair cells decline over time, while those with short bundles and basolateral processes, characteristic of type II hair cells, increase (Golub et al., 2012). Here, we show that hair cells that regenerate naturally in adult mice acquire ultrastructural and physiological properties within the ranges found in wild-type type II hair cells, including stereocilia heights and diameters, and the voltage dependence and kinetics of whole-cell voltage-gated K^+ currents (Figs. 3-6). Furthermore, no regenerated hair cells acquired the distinctive low-voltage-activated K^+ conductance (Fig. 11B, surviving type I cell) or the afferent calyx (Figs. 1, 11) of mature type I hair cells.

At 28–42 d post-DT, regenerated hair cells had immature properties, including short, thin stereocilia (Figs. 2, 4), fewer-than-normal numbers of synaptic ribbons, and higher-than-normal numbers of ribbon precursors (Fig. 9). By 170 d post-DT, regenerated hair cells had acquired several properties consistent with a mature type II state. Bundles had adopted planar cell polarity and established appropriate orientation (Fig. 3). By 70 d post-DT, bundle heights fell within the range of normal type II hair cells (Fig. 4) as described by Li et al. (2008). Hair bundle displacements evoked transduction currents in regenerated hair cells with operating ranges and polarities expected based on wild-type type II hair cells (Fig. 5). Outward K^+ currents, which dominate the voltage-activated basolateral currents, had similar conductance densities (conductance per unit surface area) in WT type II and regenerated hair cells (Fig. 6). Regenerated hair cells acquired mature-appearing efferent and afferent synapses (Figs. 8, 10), and presynaptic ribbons had normal density along

the basolateral processes and normal colocalization extent with postsynaptic glutamate receptors (Fig. 8). These results show that the lack of vestibular systems-level recovery did not reflect the absence of either hair cell mechanosensitivity or synaptic structures in the regenerated hair cells.

In summary, the hundreds of hair cells in adult mouse utricles that regenerate following DT treatment acquired several mature ultrastructural, morphologic, and physiological attributes of type II hair cells. Immature properties persisted, however, in some regenerated hair cells. Relative to mature WT type II hair cells, regenerated hair cells were, on average, smaller (Fig. 6D) and had smaller transduction currents (Fig. 5F). They were also more likely to express Na_V currents and to have small HCN currents or none at all (Fig. 7). We could not determine the age of each regenerated hair cell, but immature properties persisted well after 70 d post-DT, when new hair cells had stopped increasing in number.

Does the lack of systems-level recovery in DTR mice imply that type II hair cells contribute little to recognized vestibular functions? We do not have strong hypotheses for type II-specific vestibular functions: while afferent physiological properties differ markedly by innervation zone (striola vs extrastriola), the specific contributions of type I and II hair cells are not clear because, in mammals, both hair cell types reside in both zones and most afferent neurons innervate both hair cell types (for review, see Goldberg, 2000). Some insights are provided by studies in which avian vestibular epithelia were damaged with ototoxic antibiotics, causing loss and regeneration of both hair cell types and substantial, though incomplete, functional recovery. In pigeons, there was significant recovery of gaze-stabilizing vestibular reflexes before the late restoration of calyces (Haque et al., 2008, 2009). This early recovery was mediated by hair cells transmitting via bouton synapses, which included type II cells but presumably also nascent type I cells that were eventually enveloped by calyces. The delayed restoration of calyces coincided with expansion of the frequency range of gaze stabilization. In chickens, the recovery of VOR and vestibulocollic reflex (VCR) gains correlated better with the number of hair cells innervated by calyces than with other hair cells (Carey et al., 1996; Goode et al., 1999). These observations suggest that type II hair cell–bouton and type I hair cell–calyx pairings both make significant contributions toward recovery of systems-level function. In DTR mice, then, lack of systems-level recovery may reflect a failure to replace the full variety of mature phenotypes, including type I hair cells with calyces, but plausibly also certain type II hair cells.

Additionally or alternatively, a lack of systems-level recovery may reflect the large (~80%) reduction of total hair cell inputs. Given that head motions normally coactivate many hair cells of both types, downstream circuitry may require strong convergence of afferent signals. Indeed, VCR recovery in chickens was well correlated with the total number of hair cells (Goode et al., 1999).
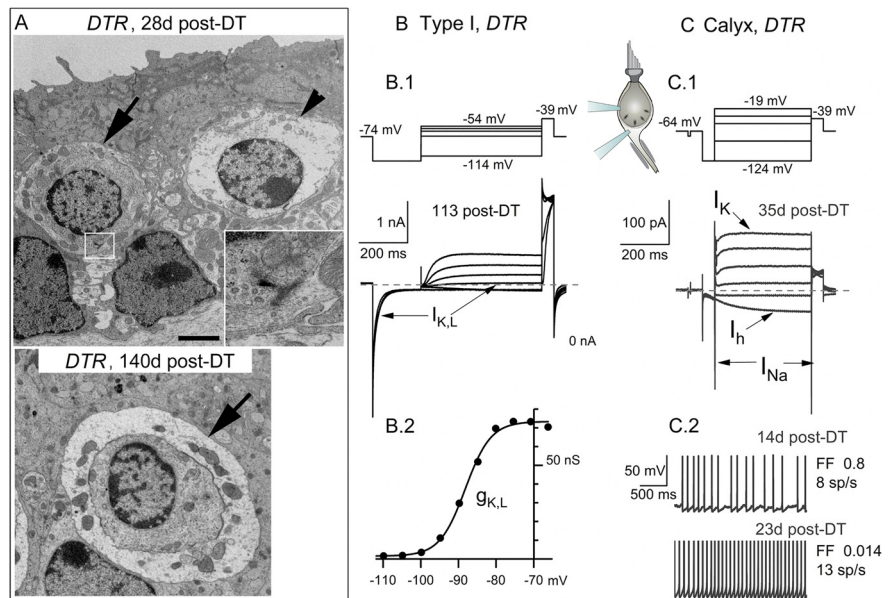
Figure 11. A small number of type I hair cells and calyces in DTR utricles survived DT treatment and appeared normal. *A*, TEM of healthy-appearing type I hair cells and calyces (arrows) at early (top) and later (bottom) times post-DT treatment. A presynaptic ribbon (box, top) is magnified in the inset. Top, Arrowhead, Type I hair cell undergoing cytolysis. Scale bar: top, 2.5 μm; (in top) bottom, 2.2 μm. *B*, *C*, Whole-cell voltage-gated currents from surviving type I hair cell (*B.1*) and calyx terminal (*C.1*) in DTR utricles. Voltage protocols (top) evoked currents (shown below voltages) with normal time course and voltage dependence. *B.2*, $G(V)$ relationship for cell in *B.1*, fit with Equation 1 (Boltzmann function) with $V_{1/2} = -78$ mV, $S = 6$ mV, $G_{max} = 47$ nS, which are consistent with normal values for $g_{K,L}$. *C.2*, Spontaneous spiking in two calyceal terminals with different rates [spikes per second (sp/s)] and regularity of spike intervals [measured by Fano Factor (FF)].

Regenerative capacity in mammalian vestibular organs diminishes with age in both quantity and diversity

In contrast to our results with adult tissue, Wang et al. (2019) found that, when mouse utricular hair cells are destroyed at P1, a small number of type I-like hair cells are regenerated in addition to type II hair cells, all regenerated hair cells lose their Na_V currents with time, and there is partial recovery of acceleration-evoked potentials (i.e., VsEPs). Together with our findings, it is clear that the regenerative capacity of vestibular epithelia decreases significantly in mammals as they age. Production of type I hair cells during development is largely restricted to the embryonic period, but about half of type II hair cells are born postnatally (McInturff et al., 2018; Wang et al., 2019; Warchol et al., 2019). Type II (but not type I) production continues at a low rate in adulthood as part of normal cell turnover (Bucks et al., 2017). The failure in mature mice to generate type I hair cells either during normal turnover or after hair cell destruction may reflect maturational shifts in cell lineages for type I and type II cells and/or in responsiveness to regulatory signals. Consistent with the latter, supporting cells respond differently to damage according to age: neonatal supporting cells upregulate the Wnt pathway protein Lgr5 before regenerating both type I and type II hair cells, while older supporting cells do not upregulate Lgr5 and regenerate only type II hair cells (Wang et al., 2015). Single-cell transcriptomics may help to identify subsets of supporting cells with unique potential for generating type I versus type II hair cells, as well as signals that regulate cell fate determination.

References

Agrawal Y, Carey JP, Della Santina CC, Schubert MC, Minor LB (2009) Disorders of balance and vestibular function in US adults: data from the National Health and Nutrition Examination Survey, 2001-2004. Arch Intern Med 169:938–944.

Barry PH (1994) JPCalc, a software package for calculating liquid junction potential corrections in patch-clamp, intracellular, epithelial and bilayer measurements and for correcting junction potential measurements. J Neurosci Methods 51:107–116.

Beurg M, Fettiplace R (2017) PIEZO2 as the anomalous mechanotransducer channel in auditory hair cells. J Physiol 595:7039–7048.

Brichta AM, Aubert A, Eatock RA, Goldberg JM (2002) Regional analysis of whole cell currents from hair cells of the turtle posterior crista. J Neurophysiol 88:3259–3278.

Brugeaud A, Travo C, Demêmes D, Lenoir M, Llorens J, Puel JL, Chabbert C (2007) Control of hair cell excitability by vestibular primary sensory neurons. J Neurosci 27:3503–3511.

Bucks SA, Cox BC, Vlosich BA, Manning JP, Nguyen TB, Stone JS (2017) Supporting cells remove and replace sensory receptor hair cells in a balance organ of adult mice. Elife 6:e18128.

Burns JC, Stone JS (2017) Development and regeneration of vestibular hair cells in mammals. Semin Cell Dev Biol 65:96–105.

Carey JP, Fuchs AF, Rubel EW (1996) Hair cell regeneration and recovery of the vestibuloocular reflex in the avian vestibular system. J Neurophysiol 76:3301–3312.

Chabbert C, Mechaly I, Sieso V, Giraud P, Brugeaud A, Lehouelleur J, Couraud F, Valmier J, Sans A (2003) Voltage-gated Na+ channel activation induces both action potentials in utricular hair cells and brain-derived neurotrophic factor release in the rat utricle during a restricted period of development. J Physiol 553:113–123.

Contini D, Price SD, Art JJ (2017) Accumulation of K+ in the synaptic cleft modulates activity by influencing both vestibular hair cell and calyx afferent in the turtle. J Physiol 595:777–803.

Corey DP, Hudspeth AJ (1980) Mechanical stimulation and micromanipulation with piezoelectric bimorph elements. J Neurosci Methods 3:183–202.

Correia MJ, Lang DG (1990) An electrophysiological comparison of solitary type I and type II vestibular hair cells. Neurosci Lett 116:106–111.

Denman-Johnson K, Forge A (1999) Establishment of hair bundle polarity and orientation in the developing vestibular system of the mouse. J Neurocytol 28:821–835.

Eatock RA, Hurley KM (2003) Functional development of hair cells. In: Development of the auditory and vestibular systems 3: molecular development of the inner ear (Romand R, Varela-Nieto I, eds), pp 389–448. San Diego: Academic.

Eatock RA, Songer JE (2011) Vestibular hair cells and afferents: two channels for head motion signals. Annu Rev Neurosci 34:501–534.

Erkman L, McEvilly RJ, Luo L, Ryan AK, Hooshmand F, O'Connell SM, Keithley EM, Rapaport DH, Ryan AF, Rosenfeld MG (1996) Role of transcription factors Brn-3.1 and Brn-3.2 in auditory and visual system development. Nature 381:603–606.

Forge A, Li L, Corwin JT, Nevill G (1993) Ultrastructural evidence for hair cell regeneration in the mammalian inner ear. Science 259:1616–1619.

Forge A, Li L, Nevill G (1998) Hair cell recovery in the vestibular sensory epithelia of mature guinea pigs. J Comp Neurol 397:69–88.

Géléoc GS, Holt JR (2003) Developmental acquisition of sensory transduction in hair cells of the mouse inner ear. Nat Neurosci 6:1019–1020.

Géléoc GS, Lennan GW, Richardson GP, Kros CJ (1997) A quantitative comparison of mechanoelectrical transduction in vestibular and auditory hair cells of neonatal mice. Proc Biol Sci 264:611–621.

Géléoc GS, Risner JR, Holt JR (2004) Developmental acquisition of voltage-dependent conductances and sensory signaling in hair cells of the embryonic mouse inner ear. J Neurosci 24:11148–11159.

Goldberg JM (2000) Afferent diversity and the organization of central vestibular pathways. Exp Brain Res 130:277–297.

Golub JS, Tong L, Ngyuen TB, Hume CR, Palmiter RD, Rubel EW, Stone JS (2012) Hair cell replacement in adult mouse utricles after targeted ablation of hair cells with diphtheria toxin. J Neurosci 32:15093–15105.

Goode CT, Carey JP, Fuchs AF, Rubel EW (1999) Recovery of the vestibulocolic reflex after aminoglycoside ototoxicity in domestic chickens. J Neurophysiol 81:1025–1035.

Goodyear RJ, Kros CJ, Richardson GP (2006) The development of hair cells in the inner ear. In: Vertebrate Hair Cells. (Eatock RA, Fay RR, Popper AN, eds), pp 20–94. New York: Springer.

Groves AK (2010) The challenge of hair cell regeneration. Exp Biol Med (Maywood) 235:434–446.

Haque A, Zakir M, Dickman JD (2008) Recovery of gaze stability during vestibular regeneration. J Neurophysiol 99:853–865.

Haque A, Zakir M, Dickman JD (2009) Regeneration of vestibular horizontal semicircular canal afferents in pigeons. J Neurophysiol 102:1274–1286.

Hicks KL, Wisner SR, Cox BC, Stone JS (2020) Atoh1 is required in supporting cells for regeneration of vestibular hair cells in adult mice. Hear Res 385:107838.

Hirvonen M, Aalto H, Migliaccio AA, Hirvonen TP (2007) Motorized head impulse rotator for horizontal vestibulo-ocular reflex: normal responses. Arch Otolaryngol Head Neck Surg 133:157–161.

Hoffman LF, Choy KR, Sultemeier DR, Simmons DD (2018) Oncomodulin expression reveals new insights into the cellular organization of the murine utricle striola. J Assoc Res Otolaryngol 19:33–51.

Holt JR, Corey DP, Eatock RA (1997) Mechanoelectrical transduction and adaptation in hair cells of the mouse utricle, a low-frequency vestibular organ. J Neurosci 17:8739–8748.

Holt JR, Vollrath MA, Eatock RA (1999) Stimulus processing by type II hair cells in the mouse utricle. Ann N Y Acad Sci 871:15–26.

Horwitz GC, Risner-Janiczek JR, Jones SM, Holt JR (2011) HCN channels expressed in the inner ear are necessary for normal balance function. J Neurosci 31:16814–16825.

Horwitz GC, Risner-Janiczek JR, Holt JR (2014) Mechanotransduction and hyperpolarization-activated currents contribute to spontaneous activity in mouse vestibular ganglion neurons. J Gen Physiol 143:481–497.

Jeng JY, Carlton AJ, Johnson SL, Brown SDM, Holley MC, Bowl MR, Marcotti W (2021) Biophysical and morphological changes in inner hair cells and their efferent innervation in the ageing mouse cochlea. J Physiol 599:269–287. 2021

Kawamoto K, Izumikawa M, Beyer LA, Atkin GM, Raphael Y (2009) Spontaneous hair cell regeneration in the mouse utricle following gentamicin ototoxicity. Hear Res 247:17–26.

Lambert PR, Gu R, Corwin JT (1997) Analysis of small hair bundles in the utricles of mature guinea pigs. Am J Otol 18:637–643.

Lennan GW, Steinacker A, Lehouelleur J, Sans A (1999) Ionic currents and current-clamp depolarisations of type I and type II hair cells from the developing rat utricle. Pflugers Arch 438:40–46.

Lenoir M, Shnerson A, Pujol R (1980) Cochlear receptor development in the rat with emphasis on synaptogenesis. Anat Embryol (Berl) 160:253–262.

Li A, Xue J, Peterson EH (2008) Architecture of the mouse utricle: macular organization and hair bundle heights. J Neurophysiol 99:718–733.

Lin V, Golub JS, Nguyen TB, Hume CR, Oesterle EC, Stone JS (2011) Inhibition of Notch activity promotes nonmitotic regeneration of hair cells in the adult mouse utricles. J Neurosci 31:15329–15339.

Lysakowski A, Goldberg JM (1997) A regional ultrastructural analysis of the cellular and synaptic architecture in the chinchilla cristae ampullares. J Comp Neurol 389:419–443.

Martinez-Monedero R, Liu C, Weisz C, Vyas P, Fuchs PA, Glowatzki E (2016) GluA2-containing AMPA receptors distinguish ribbon-associated from ribbonless afferent contacts on rat cochlear hair cells. eNeuro 3: ENEURO.0078-16.2016.

McGrath J, Roy P, Perrin BJ (2017) Stereocilia morphogenesis and maintenance through regulation of actin stability. Semin Cell Dev Biol 65:88–95.

McInturff S, Burns JC, Kelley MW (2018) Characterization of spatial and temporal development of Type I and Type II hair cells in the mouse utricle using new cell-type-specific markers. Biol Open 7:bio038083.

Meredith FL, Rennie KJ (2016) Channeling your inner ear potassium: K$^+$ channels in vestibular hair cells. Hear Res 338:40–51.

Mock BE, Vijayakumar S, Pierce J, Jones TA, Jones SM (2016) Differential effects of Cdh23(753A) on auditory and vestibular functional aging in C57BL/6J mice. Neurobiol Aging 43:13–22.

Nordemar H (1983) Postnatal development of the vestibular sensory epithelium in the mouse. Acta Otolaryngol 96:447–456.

Ono K, Keller J, López Ramírez O, González Garrido A, Zobeiri OA, Chang HHV, Vijayakumar S, Ayiotis A, Duester G, Della Santina CC, Jones SM, Cullen KE, Eatock RA, Wu DK (2020) Retinoic acid degradation shapes zonal development of vestibular organs and sensitivity to transient linear accelerations. Nat Commun 11:63.

Puel JL, Saffiedine S, Gervais d'Aldin C, Eybalin M, Pujol R (1995) Synaptic regeneration and functional recovery after excitotoxic injury in the guinea pig cochlea. C R Acad Sci III 318:67–75.

Pujol R, Lavigne-Rebillard M, Lenoir M (1997) Development of sensory and neural structures in the mammalian cochlea. In: Development of the

auditory system (Rubel EW, Popper AN, Fay RR, eds), pp 146–192. New York: Springer.

Pujol R, Pickett SB, Nguyen TB, Stone JS (2014) Large basolateral processes on type II hair cells are novel processing units in mammalian vestibular organs. J Comp Neurol 522:3141–3159.

Rauch SD, Velazquez-Villaseñor L, Dimitri PS, Merchant SN (2001) Decreasing hair cell counts in aging humans. Ann N Y Acad Sci 942:220–227.

Regus-Leidig H, Tom Dieck S, Specht D, Meyer L, Brandstätter JH (2009) Early steps in the assembly of photoreceptor ribbon synapses in the mouse retina: the involvement of precursor spheres. J Comp Neurol 512:814–824.

Rennie KJ, Correia MJ (1994) Potassium currents in mammalian and avian isolated type I semicircular canal hair cells. J Neurophysiol 71:317–329.

Rennie KJ, Ricci AJ, Correia MJ (1996) Electrical filtering in gerbil isolated type I semicircular canal hair cells. J Neurophysiol 75:2117–2123.

Ruel J, Wang J, Rebillard G, Eybalin M, Lloyd R, Pujol R, Puel JL (2007) Physiology, pharmacology and plasticity at the inner hair cell synaptic complex. Hear Res 227:19–27.

Rüsch A, Eatock RA (1996) A delayed rectifier conductance in type I hair cells of the mouse utricle. J Neurophysiol 76:995–1004.

Rüsch A, Lysakowski A, Eatock RA (1998) Postnatal development of type I and type II hair cells in the mouse utricle: acquisition of voltage-gated conductances and differentiated morphology. J Neurosci 18:7487–7501.

Sadeghi SG, Pyott SJ, Yu Z, Glowatzki E (2014) Glutamatergic signaling at the vestibular hair cell calyx synapse. J Neurosci 34:14536–14550.

Sayyid ZN, Wang T, Chen L, Jones SM, Cheng AG (2019) Atoh1 directs regeneration and functional recovery of the mature mouse vestibular system. Cell Rep 28:312–324.e4.

Schug N, Braig C, Zimmermann U, Engel J, Winter H, Ruth P, Blin N, Pfister M, Kalbacher H, Knipper M (2006) Differential expression of otoferlin in brain, vestibular system, immature and mature cochlea of the rat. Eur J Neurosci 24:3372–3380.

Slowik AD, Bermingham-McDonogh O (2013) Hair cell generation by notch inhibition in the adult mammalian cristae. J Assoc Res Otolaryngol 14:813–828.

Sobkowicz HM, Rose JE, Scott GE, Slapnick SM (1982) Ribbon synapses in the developing intact and cultured organ of Corti in the mouse. J Neurosci 2:942–957.

Songer JE, Eatock RA (2013) Tuning and timing in mammalian type I hair cells and calyceal synapses. J Neurosci 33:3706–3724.

Staecker H, Praetorius M, Baker K, Brough DE (2007) Vestibular hair cell regeneration and restoration of balance function induced by math1 gene transfer. Otol Neurotol 28:223–231.

Suli A, Pujol R, Cunningham DE, Hailey DW, Prendergast A, Rubel EW, Raible DW (2016) Innervation regulates synaptic ribbons in lateral line mechanosensory hair cells. J Cell Sci 129:2250–2260.

Taylor RR, Jagger DJ, Saeed SR, Axon P, Donnelly N, Tysome J, Moffatt D, Irving R, Monksfield P, Coulson C, Freeman SR, Lloyd SK, Forge A (2015) Characterizing human vestibular sensory epithelia for experimental studies: new hair bundles on old tissue and implications for therapeutic interventions in ageing. Neurobiol Aging 36:2068–2084.

Taylor RR, Filia A, Paredes U, Asai Y, Holt JR, Lovett M, Forge A (2018) Regenerating hair cells in vestibular sensory epithelia from humans. Elife 7:e34817.

Tsuji K, Velázquez-Villaseñor L, Rauch SD, Glynn RJ, Wall C, Merchant SN (2000) Temporal bone studies of the human peripheral vestibular system. Aminoglycoside ototoxicity. Ann Otol Rhinol Laryngol Suppl 181:20–25.

Uthaiah RC, Hudspeth AJ (2010) Molecular anatomy of the hair cell's ribbon synapse. J Neurosci 30:12387–12399.

Van Hecke R, Van Rompaey V, Wuyts FL, Leyssens L, Maes L (2017) Systemic aminoglycosides-induced vestibulotoxicity in humans. Ear Hear 38:653–662.

Vollrath MA, Eatock RA (2003) Time course and extent of mechanotransducer adaptation in mouse utricular hair cells: comparison with frog saccular hair cells. J Neurophysiol 90:2676–2689.

Wang T, Chai R, Kim GS, Pham N, Jansson L, Nguyen DH, Kuo B, May LA, Zuo J, Cunningham LL, Cheng AG (2015) Lgr5+ cells regenerate hair cells via proliferation and direct transdifferentiation in damaged neonatal mouse utricle. Nat Commun 6:6613.

Wang T, Niwa M, Sayyid ZN, Hosseini DK, Pham N, Jones SM, Ricci AJ, Cheng AG (2019) Uncoordinated maturation of developing and regenerating postnatal mammalian vestibular hair cells. PLoS Biol 17:e3000326.

Warchol ME, Lambert PR, Goldstein BJ, Forge A, Corwin JT (1993) Regenerative proliferation in inner ear sensory epithelia from adult guinea pigs and humans. Science 259:1619–1622.

Warchol ME, Massoodnia R, Pujol R, Cox BC, Stone JS (2019) Development of hair cell phenotype and calyx nerve terminals in the neonatal mouse utricle. J Comp Neurol 527:1913–1928.

Wooltorton JR, Gaboyard S, Hurley KM, Price SD, Garcia JL, Zhong M, Lysakowski A, Eatock RA (2007) Developmental changes in two voltage-dependent sodium currents in utricular hair cells. J Neurophysiol 97:1684–1704.

Xiang M, Gan L, Li D, Chen ZY, Zhou L, O'Malley BW, Klein W, Nathans J (1997) Essential role of POU-domain factor Brn-3c in auditory and vestibular hair cell development. Proc Natl Acad Sci U S A 94:9445–9450.